Emplacement of laboratory igneous sheets and fingers influenced by the Mohr-Coulomb properties of the host

Frank Guldstrand[1], Alban Souche[1], Håvard Svanes Bertelsen[1], Alain Zanella[2], and Olivier Galland[1]*

*Corresponding Author: olivier.galland@geo.uio.no

[1]Physics of Geological Processes (PGP), The NJORD Centre, Dept of Geosciences UiO, Oslo, Norway,

[2]Le Mans Université, Géosciences Le Mans - LPG UMR 6112, 72085, Le Mans, France

Keywords*:* Magma Emplacement, Dyke, Sheet intrusion, Finger intrusion, Host Rock Deformation, 2D Laboratory Model

Abstract

Planar magma intrusions such as dykes and sills are major magma transport features and the main feeders of volcanic eruptions. Among planar intrusions, sheet intrusions are fracture-like continuous conduits, which are assumed to form by tensile opening and dominantly elastic deformation of the host. However, numerous planar intrusions are not continuous, and consist of aligned finger-shaped or more lobate conduits. Field observations show that the emplacement of these fingers is associated with inelastic, shear failure of the host rock, suggesting that the Mohr-Coulomb properties of crustal rocks play a significant role in the emplacement of fingers. In this study, we test the effects of the Mohr-Coulomb properties of crustal rocks on the emplacement of sheet-shaped and finger-shaped intrusions through quantitative 2-dimensional laboratory experiments. The model magma is viscous Golden Syrup, and the model rock is made of mixtures of dry granular materials of variable cohesion. A sideview camera allows monitoring the shape of the propagating intrusions and the associated deformation in the host, and a pressure sensor monitors the pressure of the syrup. Our experiments show that sheet intrusions form in high-cohesion hosts whereas finger-shaped intrusions form in low-cohesion hosts. Deformation analysis of the host and pressure data show that the sheets and fingers result from drastically distinct dynamics: sheets dominantly propagate as a fracture, whereas fingers are emplaced as viscous indenters.

All in all, our experiments highlight that the cohesion of the Earth's crust and the associated shear damage play a major role on planar intrusion emplacement.

Introduction

The emplacement of dykes and sills in the Earth's crust is a fundamental process in the transport of magma and feeding volcanic eruptions [*Halls and Fahrig*, 1987; *Rivalta et al.*, 2015; *Tibaldi*, 2015; *Magee et al.*, 2016; *Galland et al.*, 2018]. Understanding the emplacement mechanics of magmatic intrusions allows for an improved understanding of the Earth system, but it is also of applied importance in terms of hazard mitigation and natural resource exploration [*Senger et al.*, 2017; *Guldstrand et al.*, 2018; *Rabbel et al.*, 2018]. Dykes and sills usually overall exhibit long and thin planar shapes, i.e., igneous sheets, similar to those of fractures. Based on this resemblance, most dyke and sill emplacement models have assumed that they form as tensile fractures propagating through elastic medium [e.g. *Pollard*, 1987; *Bunger and Cruden*, 2011; *Galland and Scheibert*, 2013; *Rivalta et al.*, 2015]. According to this mechanism, dykes and sills are expected to be continuous and to exhibit sharp tips accommodating tensile opening of the host rock, as supported by field observations [Figure 1; *Galland et al.*, 2018; *Poppe et al.*, 2020].

All planar intrusions emplaced in the brittle crust, however, do not exhibit shapes and structures that are compatible with the sheet intrusion emplacement mechanism. For example, numerous igneous sills exhibit lobate morphologies, so-called finger shapes [*Pollard et al.*, 1975; *Schofield et al.*, 2012; *Galland et al.*, 2019]. Detailed field observations and 3D seismic data analysis of fingers show that even if the overall apparent shapes of these intrusions look like sheets, they are discontinuous and the tips of individual segments are blunt, i.e. everything but sharp [*Pollard et al.*, 1975; *Schofield et al.*, 2012; *Spacapan et al.*, 2017; *Galland et al.*, 2019; *Kjøll et al.*, 2019]. In addition, the visible structures accommodating the propagation of the fingers' tips dominantly exhibit shear, compressional failure of the host rock [*Pollard et al.*, 1975; *Duffield et al.*, 1986; *Spacapan et al.*, 2017; *Galland et al.*, 2019].

The structural differences between sheet- and finger-shaped intrusions resides principally in contrasting mechanical behaviors of their host rock, especially on their failure modes (tensile versus shear). Tensile and shear failure modes are fundamental

features of the Mohr-Coulomb-Griffith failure criteria of brittle rocks, and their occurrence depends on parameters such as rock cohesion and angle of friction [Fig. 1; *Jaeger et al.*, 2009; *Abdelmalak et al.*, 2016]. The different failure modes associated with sheet and finger intrusions leads to the main working hypothesis this paper intends to test: Mohr-Coulomb properties of crustal rocks, and in particular their cohesion, control the emplacement of igneous sheets versus igneous fingers.

We propose to test this hypothesis through quantitative quasi-2D laboratory models of model magma intrusion with strong (high cohesion) to weak (low cohesion) model host rocks. The model magma used was viscous golden syrup injected at a constant flow rate at room temperature with pressure monitored at the inlet. In order to decipher between distinctive deformation modes accommodating the emplacement of the syrup, the model rock displacements were monitored using a Digital Image Correlation (DIC) algorithm available through the open source photogrammetric structure-from-motion software MicMac [*Galland et al.*, 2016]. Our results show that cohesion has a significant control on the emplacement mechanics on the intrusion of a viscous fluid. Higher cohesion hosts result in sheet emplacement while lower cohesion hosts result in the emplacement of finger intrusions with drastically different emplacement mechanics at work evident in deformation and pressure monitoring.

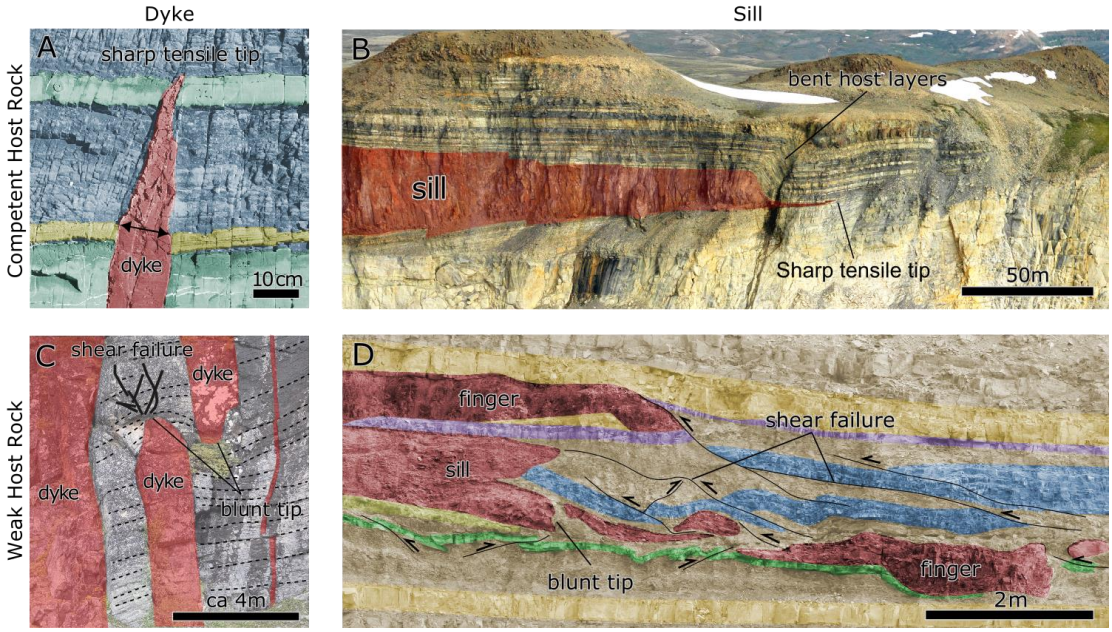

Figure 1. A,B sharp tipped tensile sheet intrusions into competent host rock. C,D Blunt tipped intrusions associated with shear failure into weak host rock [*Spacapan et al.*, 2017; *Galland et al.*, 2018; *Kjøll et al.*, 2019; *Poppe et al.*, 2020].

Method

Experimental setup

The experimental setup is an improved version of that of *Abdelmalak et al.* [2012]. It consists of a 30 mm thick 2D Hele-Shaw cell with dimensions 80 cm wide and 50 cm high (Fig. 2). The frame consists in total of 4 separate aluminum bar profiles. Front and back glass panes are kept in place with clamps and gaskets. The inlet consists of a rectangular 1 mm wide, 3 cm high, slit in order to promote the initiation of a vertical sheet intrusion; it is an interchangeable separate piece attached to the center of the two bottom aluminum profiles. Rubber gaskets ensure a tight seal of the inlet to the glass. A simple tube system connects a syringe-pump to a pressure sensor before proceeding to the inlet. The syringe pump injects the model magma at constant volumetric flow rate.

Materials

The model host rock consists of 4 different mixes of silica flour and glass microbeads (table 1). These two fine-grained materials fail according to a Mohr-Coulomb criterion [*Abdelmalak et al.*, 2016]. The glass bead flour (GB) has a modal grain size of 30 µm and is nearly cohesionless as it collapses under its own weight. Silica flour (SF) has a modal grain size of 10-20 µm and is cohesive when compacted. As such, SF does not collapse under its own weight and sustains vertical walls [*Galland et al.*, 2006]. *Abdelmalak et al.* [2016] showed that the cohesion of GB/SF mixes follows a near linear trend with respect to mixing proportion, so that these mixes allow us to explore the effect of variable cohesion on the modeled processes. We added 7wt% of black aluminum silicate powder, with a grain size of 0.2-0.6 mm, to the flour mixes to add texture to the host. This was in order to apply Digital Image Correlation (DIC) to track the deformation induced by the propagating model magma. We tested that the addition of the tracer did not significantly affect the cohesion of the mix.

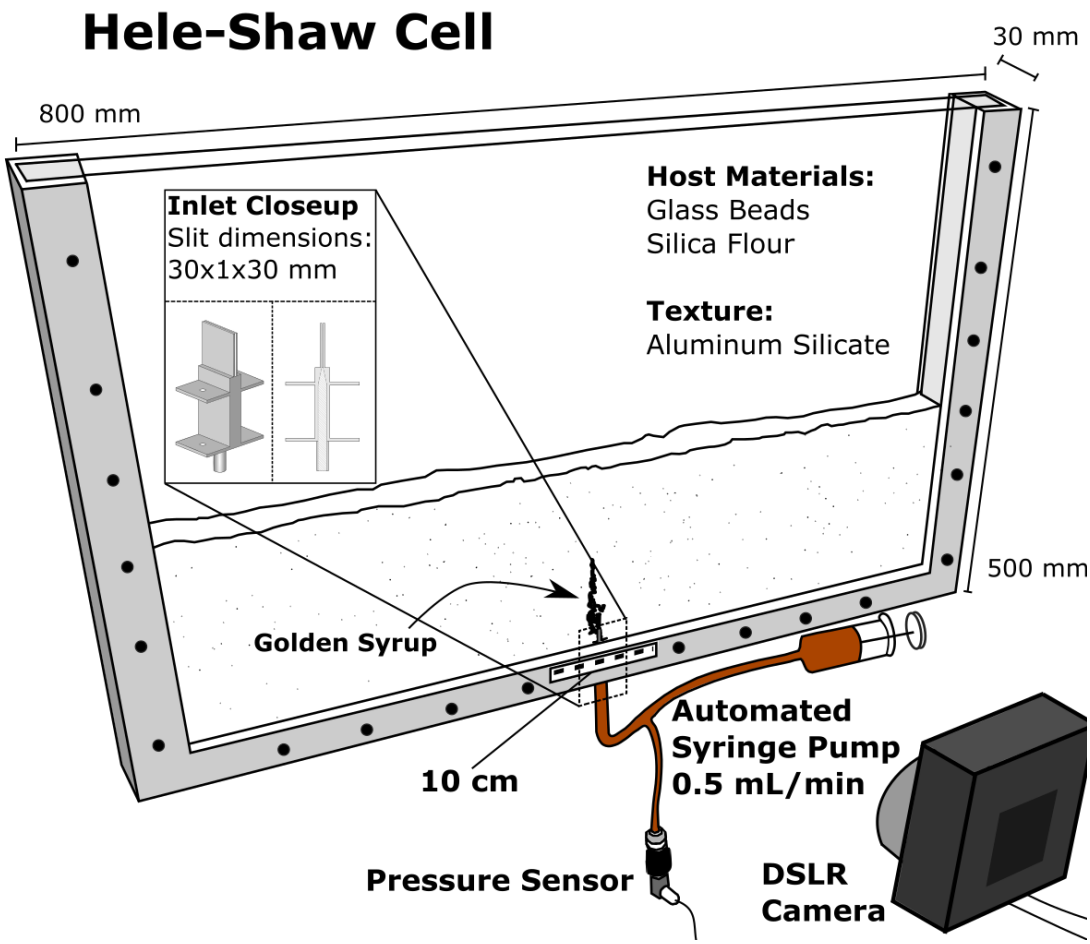

Figure 2 Dimensions of Hele-Shaw cell including a compacted mix of cohesive silica flour and glass beads into which golden syrup is injected through the use of an automated syringe pump at 0.5 ml/min. Monitoring is done through recording of pressure and a camera taking photographs each 120/180 s depending on the mix used. We then apply digital image correlation (DIC) to the series of processed images.

The model magma, Lale & Tate's Golden Syrup, is a commonly used fluid in intrusion experiments [e.g. *Mart and Dauteuil*, 2000; *Mathieu et al.*, 2008; *Delcamp et al.*, 2012]. The injection was done at room temperature (~21ºC), at which we measured the viscosity (~55 Pa s) and the density (~1440 kg m^{-3}) of the syrup. This is in agreement with reported values of *Llewellin et al.* [2002] and *Beckett et al.* [2011]. The wettability of the golden syrup was tested in combination with the silica flour, glass beads and glass by measuring the contact angle in air using the DSA drop shape analyzer from Krüss. From this we concluded that Golden Syrup was non-wetting in all cases for the time scale of an experiment. The non-wetting property and the small grain size ensure

fluid propagation occurred mainly through fracturing and pushing the host material, and not through percolation and porous flow.

The suitability of the model materials to simulate viscous magma emplacement in the brittle crust has been discussed in detail by [*Abdelmalak et al.*, 2012]. Given the size of our laboratory setup and the range of cohesion of the model crust, 1 cm in our experiment scales to 10-100 m in nature. In that scale, the high-cohesion materials simulate competent rocks (i.e. limestone, consolidated sandstone, plutonic rocks, etc.) whereas the low cohesion materials simulate weak rocks (i.e. shale, poorly consolidated sandstone, volcanic tuff, etc.) [*Abdelmalak et al.*, 2016].

Experiment Protocol

To prepare an experiment, first the inlet is plugged, and a known mass of flour is poured into the cell. The flour mix must not be poured into the cell too carefully as it will enhance sorting of the aluminum silicate grains, and so decrease the quality of the texture that is necessary for DIC. A heavy metal bar with a handle is placed on top of the flour within the cell; a water level is used to ensure that a flat and level surface is achieved. We then compact the flour using a high- frequency shaker running on compressed air (Houston Vibrator, model GT-25). The heavy metal bar was lined with a porous foam so that when lifted it did not create suction and disturbance of the compacted flour. This procedure ensures a homogeneous and repeatable compaction.

153

154 **Table 1.** Experiment parameters and model host rock properties

Exp Nr	V_{inj} (mL min^{-1})	Mix (GB/SF)	Mass (kg)	Depth (cm)	Density (kg m^{-3})	Compaction %[a]	Cohesion (Pa)[b]	Temp (C)	Erupt Time (Min)
16	0,5	90/10	7,5	16,2	1652,8	2,5	239.5	21,1	52
24	0,5	90/10	7,5	16,75	1606,7	6,0	239.5	21	77
14	0,5	80/20	7,5	16,2	1652,8	4,0	313.1	21,3	54
23	0,5	80/20	7,5	15,9	1679	10,4	313.1	20,9	48
19	0,5	50/50	6,5	16,3	1425	14,6	374.96	20,6	69
20	0,5	50/50	6,5	16,8	1388,9	13,9	374.96	21,6	82
21	0,5	0/100	4,5	14,2	1107,1	14,4	559.91	21	96
22	0,5	0/100	4,5	15,1	1052	14,6	559.91	21,5	130

155 [a]Compaction between measured and initial density and final compacted density.

156 [b]From *Abdelmalak et al.* [2016].

157

158 The amount of compaction differs between the mixes, as pure GB does not compact
159 much, whereas pure SF compacts up to ~15%. For each mix, we compacted the
160 maximum amount, a range of 3-15% compaction, resulting in final densities of 1052-
161 1652.8 kg m^{-3} (0/100 GB/SF and 90/10 GB/SF respectively). The inlet plug was
162 removed after compaction.

163 The viscous golden syrup was put into a syringe and allowed to degas during
164 the model host rock preparation. The syringe was then put into the syringe pump and
165 connected to the inlet. A pressure sensor was connected to the injection system with a
166 T-connector in-between the pump and inlet. All experiments were performed with a
167 constant flow rate of 0.5 ml min^{-1} resulting in experiment durations of ~52- 130 min.
168 The pressure data has been smoothed using a Savitsky-Golay filter applied equally to
169 all pressure data to remove oscillations inherent to the syringe pump and tube system.
170 However due to the low injection velocity and the high viscosity of the fluid we deem
171 that the effects of such oscillations are negligible.

172 A DSLR camera (NIKON D3200) took pictures of one side of the
173 experiment (Fig. 2) at constant framing rate to monitor the evolution of the model
174 dykes. The camera and pump triggers, as well as the pressure logging, were integrated
175 and synchronized via a custom designed Arduino system.

176

177 *Deformation Monitoring*

The side view photographs are used to compute maps of displacements induced by the intruding syrup within the model crust. We corrected the optical distortion of the lens by taking a series of pictures of a checkerboard, of known size, attached to the front glass plate of the cell after each experiment. The image distortion correction was calculated using the image toolbox available in MATLAB. The image toolbox also allows for adaptively adjusting the contrast of the image, enhancing the texture. We then applied DIC using the MM2DPosSism-algorithm, which has been specifically designed to detect very small displacements [*Galland et al.*, 2016]. This algorithm is available through the free open-source structure-from-motion software MicMac developed by the French National Geographic Institute IGN [*Rosu et al.*, 2015; *Rupnik et al.*, 2017]. This allows us to compute displacements smaller than 0.1 mm between images [e.g. *Galland et al.*, 2016]. The MM2DPosSism-algorithm is most successful for a given range of displacements. In order to give the best displacement results, we adjusted the temporal resolutions in our experiments. For the experiments in 90/10 and 80/20 mixes, which were shorter in duration, the temporal resolution was 120 s. The experiments in 50/50 and 0/100 mixes, which were longer in duration and of smaller displacements, the temporal resolution was 180 s.

Results

Intrusion Characteristics

We produced experiments using 4 different mixes of cohesive Mohr-Coulomb host material. Each experiment was performed twice to test the repeatability of our results. These repeated experiments exhibited consistent results with the first experiment using the same cohesion. The repeatability of this type of experiment has also been thoroughly demonstrated by *Abdelmalak et al.* [2012]. All experiments used an inlet depth of ~16 cm, except the 100% SF experiments (0/100) where the inlet depths were 14.2 and 15.1. Shallower depths were chosen as attempts at 16 cm depth failed to produce eruptions because the intrusions were significantly thicker than those in the other experiments, such that the available syrup volume in the pump was insufficient.

A typical experiment started with chaotic emplacement of the syrup, resulting in complex branching nucleating from the inlet. However, the dominant vertical flow from the inlet ultimately forced a sub-vertical intrusion to form, propagating in a relatively stable fashion. At a certain depth, the intrusion changed

behavior. Its tip either deviated from vertical (Fig. 3) or bifurcated into two small branches (Fig. 3). In the following sections, we will refer to this transition depth as the *critical depth*. Subsequently, the syrup keeps ascending until erupting at the surface. All of the intrusions were associated with uplift and surficial extensional fractures parallel to the intrusion and perpendicular to the cell. Some extensional fractures can close and migrate as the intrusion approached the surface. The intrusion could also cause the basal uplift of a block of the host. These observations are consistent with those of *Abdelmalak et al.* [2012]. Although this general description fits all our experiments the differences which will be detailed in the following paragraphs.

In the high cohesion hosts (50/50 and 0/100 mixes, Fig. 3C, D), the intrusions were planar in geometry, perpendicular to the glass walls, clearly splitting the flour in two blocks. The initial chaotic branching near the inlet was less than in the low cohesion experiments; note, however, that the bottom branches grew during the duration of the experiments. The stable ascending intrusions exhibit a clear sheet shape, unit it reached the critical depth. In the 50/50 mix experiment, the intrusion grew continuously and inclined after reaching the critical depth (Fig. 3C). Conversely, in the 0/100 mix experiment (the highest cohesion), the intrusion tip arrested at the critical depth, resulting in thickening of the sheet, until the overburden failed (Fig. 3D). At the critical depth, the intrusion tip split in two small branches (Fig. 3D middle column), and subsequently one branch took over to accommodate for the syrup propagation (Fig. 3D right column). In these experiments, significant uplift can only be seen after the intrusion crossed the critical depth.

For lower cohesion hosts (90/10 and 80/20 mixes, Fig. 3A, B), the intrusions exhibited a more undulating and branching geometry. In the experiment with the 90/10 mix, the intrusion did not appear as a perfect continuous sheet, so that it did not split the entire host in two (Fig. 3A). Instead, the intrusion exhibited a finger structure, such that blocks of the host material remained between the intrusion and glass walls. As a result, the intrusion appeared as disconnected segment along the photographed glass plate, while they were connected in the third dimension. In the experiment with the 80/20 mix, the base of the intrusion was thick enough to constitute planar sheet geometry (Fig. 3B). Significant uplift was visible already when the intrusion was at depth, i.e. under the critical depth. At the critical depth, a hybrid form of damage ahead of the intrusion was observed, i.e. distributed damage throughout the wedge of material

244 above the intrusion and small extensional open fractures at the surface. These fractures
245 were more prominent in the 80/20 mix host than in the 90/10 mix host (Fig. 3A, B).
246

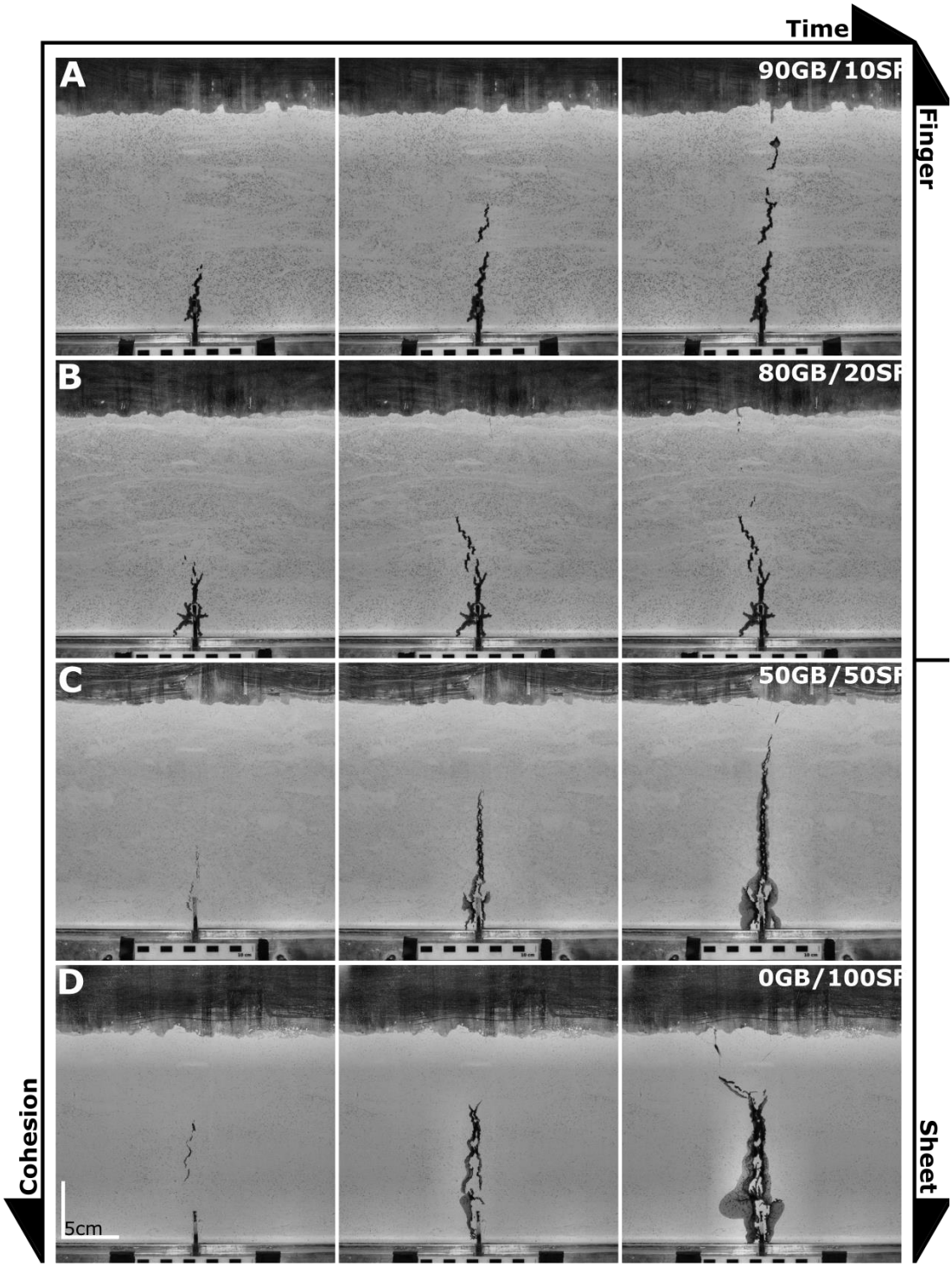

Figure 3. The rows show intrusion into a compacted mix of 90 wt% glass beads and 10% silica flour (A), 80/20 (B), 50/50 (C) and 0/100 (D). Columns show experiment photos at an initial, intermediate and late time step. The time steps were chosen such that they show intrusion initiation, a period of stable vertical propagation and the critical depth where failure of the overburden occurs. Experiments

in 50/50 (C) and 0/100 (D) comprise sheet intrusions while only the base of the 80/20 (B) intrusions are of sheet geometry. Accelerated experiment videos are available in supplemental material S1.

Propagation Velocity

The experiment durations differed, even if the injection rate was constant. The experiment duration was in general shorter for low cohesion experiments and longer for high cohesion experiments, implying distinct propagation velocities. We measured the propagation velocity of the intrusion tips using simple image analysis (Fig. 4; left column). The highest point of the intrusion was then extracted at each time step. However, in the initial and final time steps, because of the complex shapes of the intrusions, we may not adequately track the propagating tips. In addition, during the initial timesteps, the intrusion is often not yet observable. Thus, for the time steps earlier than the first visible occurrence of the liquid on the photographs, we set a constant value corresponding to the depth of the intrusion tip at its first documented position. Thus, the analysis presented in Fig. 4 (left column) is most relevant in the stable phase of propagation of the intrusion, i.e. the intermediate part. We interpolated the discrete measurements of the depth of the intrusion tips to a continuous curve (Fig. 4; red line in left column), allowing us to compute propagation velocity of the intrusion tips (Fig 4; right column).

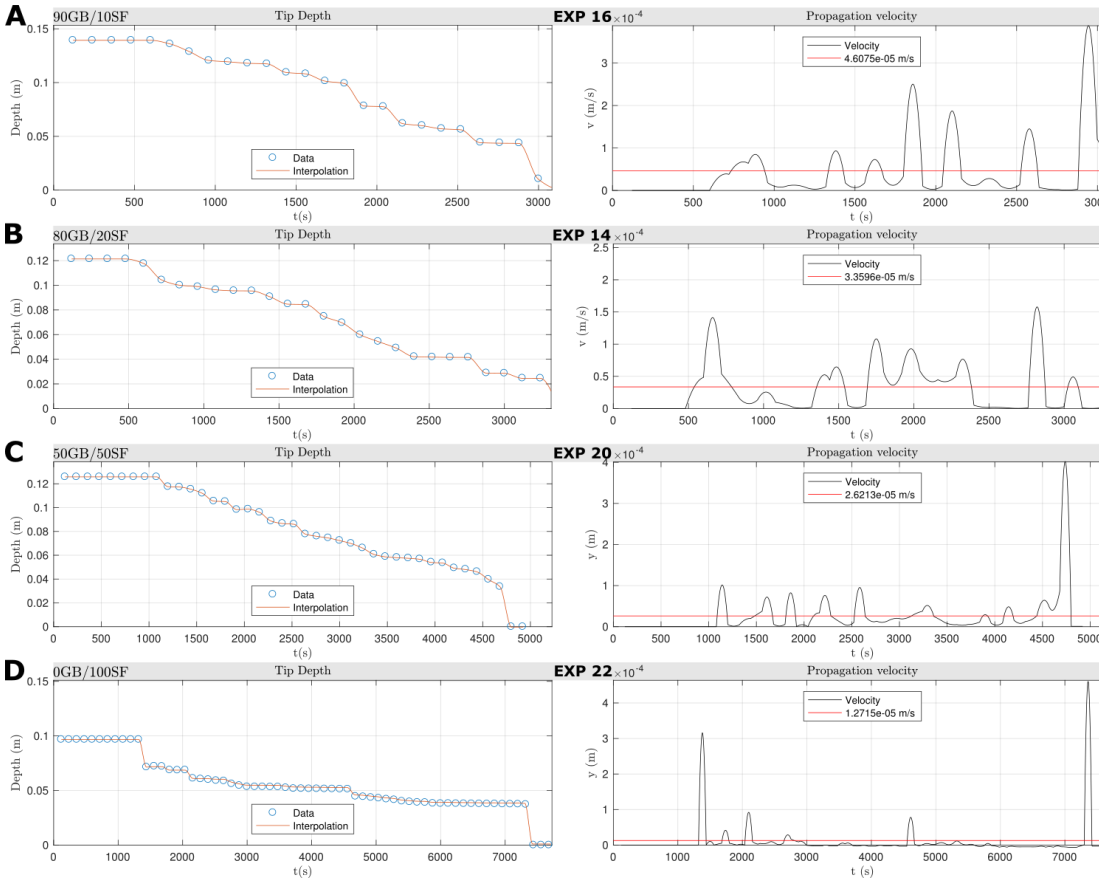

Figure 4. Left plots in each row show the depth of the intrusion tip identified in the experiment pictures using an interval of 120 s. The right plots show the vertical propagation velocity calculated from the intrusion depth and time. The average propagation velocity is plotted in red and presented in the legend. During initial time steps we cannot track the intrusion tip until the intrusion is visible therefore the initial values are set to the constant depth where the intrusion is first visible. During final time steps due to the damage created ahead of the intrusion and the creation of open fractures it also makes the intrusion difficult to track. Plots of additional experiments are available in the supplemental material S2.

The average propagation velocity (red horizontal line in right column of Fig. 4) decreases from ~0.5×10^{-5} m s^{-1} to ~0.15×10^{-5} m s^{-1} with increasing cohesion of the host material. We note as well that the propagation was not steady, with periods of slow, even no, propagation alternating with sudden accelerations, i.e. burst-like behavior. There are many more busts in the low cohesion experiments than in the high cohesion ones.

Horizontal Displacements

Figure 5 displays time series of maps of horizontal displacements U_x. In all experiments, the displacements are rightward to the right of the intrusions and leftward to the left of the intrusions, indicating opening of the host to accommodate the emplacement of the intrusions. The maximum displacement values are along the walls of the intrusions, and the displacements decrease gradually away from the intrusions, marking displacement halos on each side of the intrusions.

However, we can notice differences between the low and high cohesion experiment. In the high cohesion experiments (50/50 and 100/0), the U_x opening occurs along the entire length of the growing intrusions (Fig. 5C, D). Little or no horizontal displacement is detected in the overburden when the intrusion is below the critical depth. When the intrusion reaches the critical depth, the displacement along the deeper part of the intrusion walls decreases or ceases. From this time on, displacements mainly affect the shallower part of the host, in between the critical depth and the surface (Fig. 5C, D).

The U_x displacements in the low cohesion experiments (90/10 and 80/20), before the intrusion reaches the critical depth, concentrate in the very upper parts of the intrusions, and even extend shallower than the intrusion tips (Fig. 5A, B). Conversely, the bottom parts of the intrusions exhibit no horizontal displacement at all. After the intrusion reaches the critical depth, it triggers horizontal displacements that extended until the model surface. We note that in the early stage of the 80/20 experiment, the initial sheet triggered horizontal displacement that extended along the entire intrusion (Fig. 5B). The displacement subsequently localized close to the intrusion tip.

Videos of all horizontal displacements are available in the supplemental material S2.

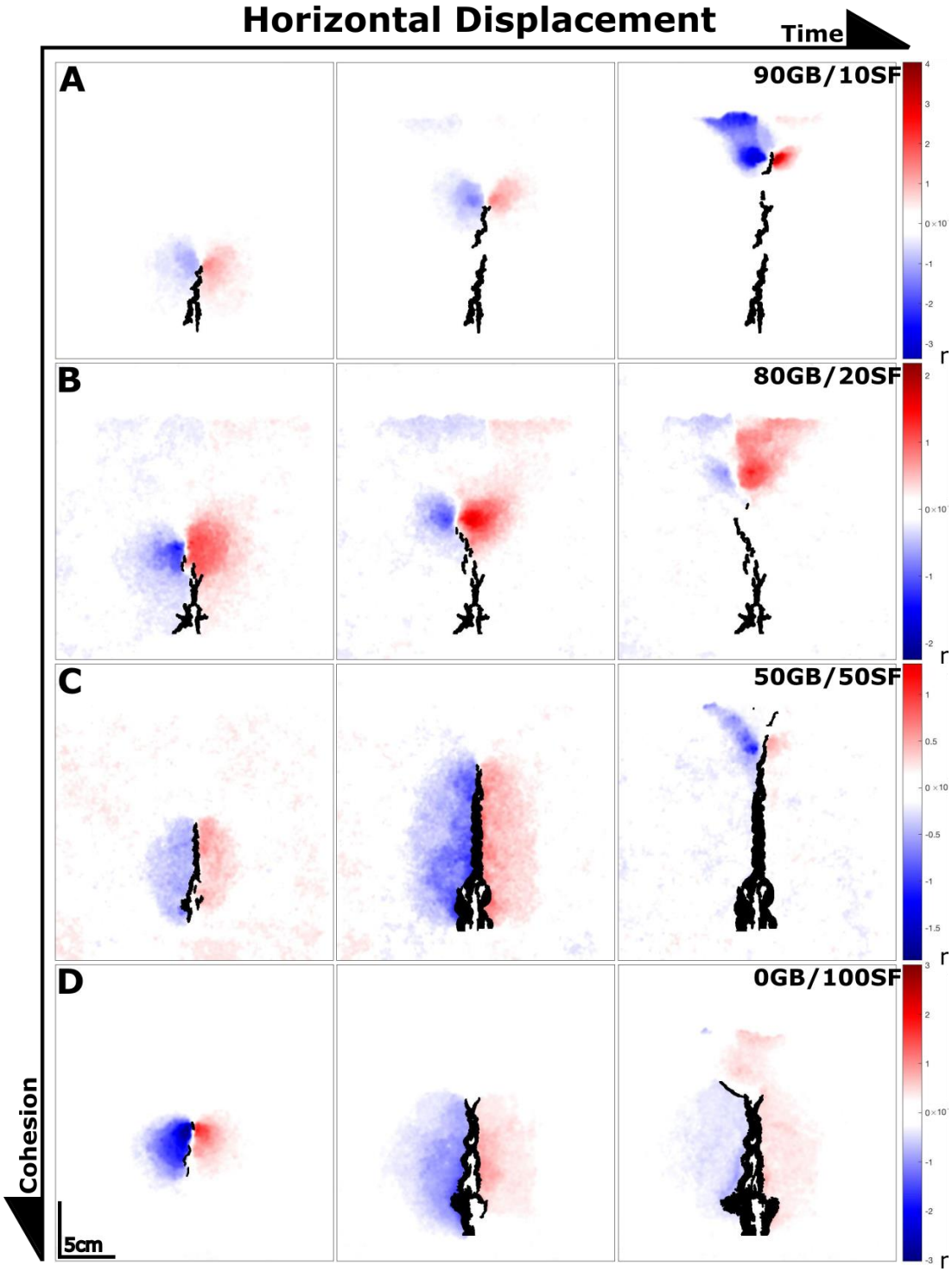

Figure 5. The rows show intrusions (black) into mixes of 90/10 (A), 80/20 (B), 50/50 (C) and 0/100 (D). Columns show experiment photos at an initial, intermediate and late time step. A and B shows that deformation, during propagation, is mainly concentrated to and beyond the intrusion tip. C and D show the entire fracture being active and displacing during vertical propagation. Once the critical depth is reached, the overburden fails and pathways were created for the fluid to utilize for the final ascent and any opening of the intrusion ceased. Accelerated experiment videos are available in supplemental material S1.

Vertical Displacements

Figure 6 displays time series maps of vertical displacement U_y. Overall, the intrusions triggered uplift only, mostly restricted in the overburden of the intrusions. In the weakest host (90/10), widespread uplift occurred above the intrusion tip already at a very early deep stage of intrusion emplacement. This uplift affected the entire overburden, from the tip of the intrusion up to the surface (Fig. 6A). The uplift magnitude increases as propagation occurs, but remains constrained above the intrusion tip. This implies that the uplifted domain reduced in size during the propagation of the intrusions. The boundaries of the uplifting domain were gradual. Once the critical depth is reached and the overburden fails, the majority of the displacements cease with the exception of minor displacements of blocks as the fluid propagates to the surface. A similar evolution is observed in the 80/20 experiment (Fig. 6B). However, the deformation field displays discontinuities that suggest the occurrence of faults that partly dissect the uplifted domain.

In the more cohesive 50/50 experiments, the early and intermediate propagation of the intrusions did not trigger significant uplift of their overburden, except small sporadic patches (Fig. 6C). However, as the intrusion tip approaches the critical depth, sudden substantial uplift affected the overburden (Fig. 6C). We notice that the center of the uplifted domain is off-centered to the left with respect to the underlying intrusion in both 50/50 experiments; in these experiments, the intrusion deviated rightward after crossing the critical depth. The 0/100 experiment displayed more prominent patches of uplift at depth until the overburden reached its critical depth (Fig. 6D). At this point there is widespread uplift dominantly above the intrusion. The repeated experiment clearly shows asymmetric uplift with one side of the host being uplifted (Supplemental material S2).

Videos of all vertical displacements are available in the supplemental material S2.

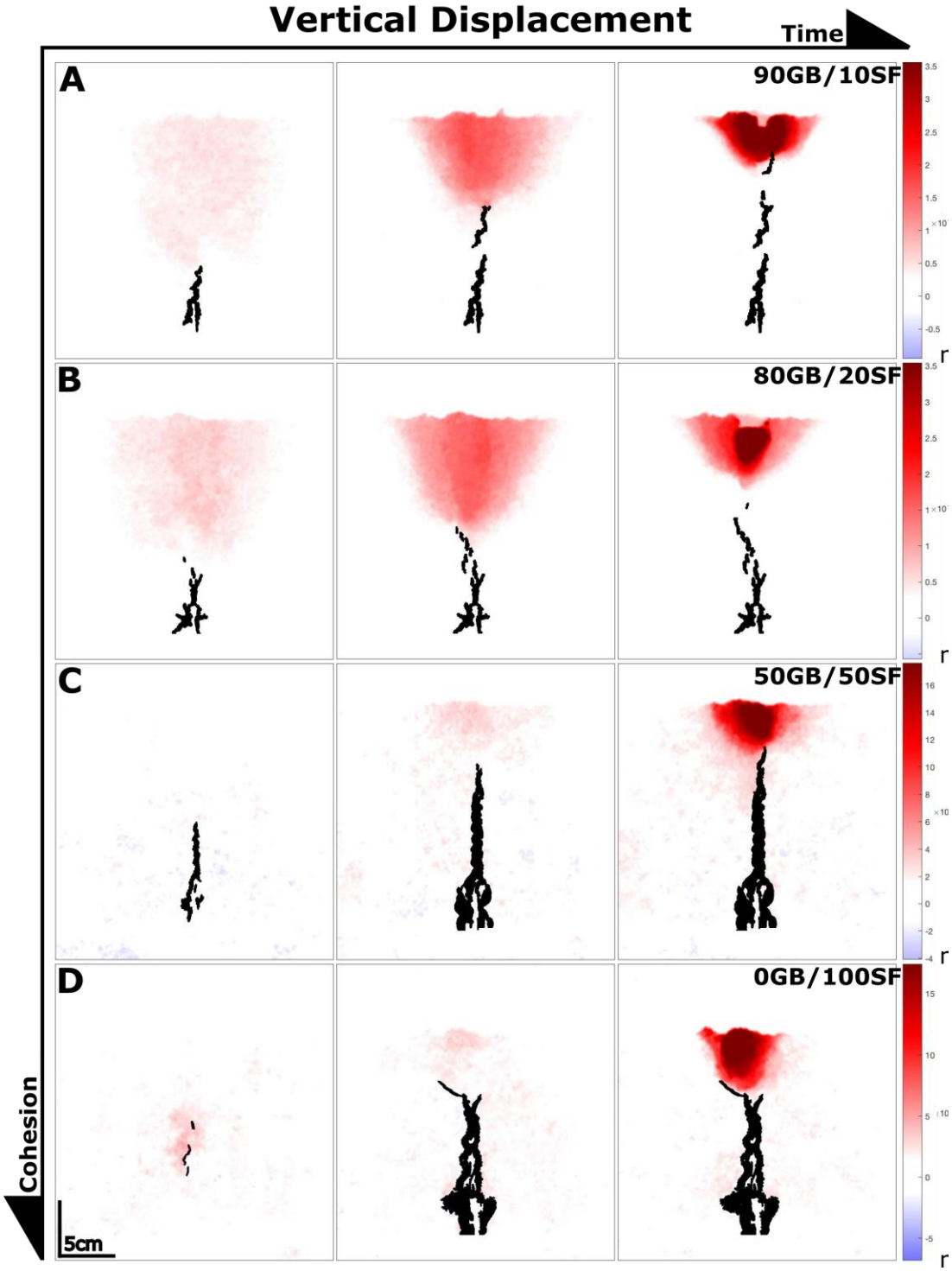

Figure 6. The rows show intrusions (black) into mixes of 90/10 (A), 80/20 (B), 50/50 (C) and 0/100 (D). Columns show experiment photos at an initial, intermediate and late time step. A and B shows that vertical displacement extends from the intrusion tip to the surface already at depth. C & D shows only small vertical displacements during propagation at depth, late intermediate stage show uplift primarily on one side of the intrusion while uplift is strongest directly above the intrusion tip. The color bar has limited in the positive value to enhance smaller uplifts at depth. Accelerated experiment videos are available in supplemental material S1.

333

334 *Shear Strain*

335 The horizontal and vertical displacement maps in the host material allow for calculating
336 time series maps of shear strain, $\gamma = \frac{1}{2}(\frac{\partial U_x}{\partial y} + \frac{\partial U_y}{\partial x})$, as the intrusion propagates (Fig. 7).
337 As the displacements are small, this analysis is prone to noise so smoothing has been
338 applied to the data before calculating the shear strain. Videos of the shear strain in all
339 the experiments are available in the supplemental material S2.

340 The experiment with the 90/10 host, i.e. low cohesion, show prominent
341 bands of reverse shear strain rooted on the intrusion tip. Already at depth, there are two
342 inclined bands extending out from the intrusion tip (Fig. 7A; left column). These shear
343 bands are persistent while the intrusion propagates upwards until the critical depth,
344 where the shear bands curve and extend from the intrusion tip to the surface, signaling
345 failure of the overburden. The shear bands display similar characteristics in the 80/20
346 mix but appear slightly larger in extent (Fig. 7B).

347 In the experiments with higher cohesion hosts (Fig. 7C, D), shear strain is
348 generally smaller in magnitude and restricted to smaller domains. Small, inclined
349 reverse shear bands extend beyond the visible intrusion tip already at depth and during
350 propagation. However, these are visible only intermittently and are shorter than in the
351 lower cohesion experiments. Sporadically, the shear bands appeared asymmetrically,
352 i.e. only the left or right shear band was visible. During propagation at depth, small
353 shear strains intermittently occurred below the intrusion tip, i.e. along the walls of the
354 dyke (Fig. 7C, D). Once the intrusion reached the critical depth, failure of the
355 overburden initiated and bands of localized shear strain emanated from the tip to the
356 intrusion to the surface (Fig. 7C, D). At this point in time, shear strains concentrate only
357 in the overburden of the intrusions and the small shear strains below the intrusion tip
358 ceased. We note as well that in the high cohesion experiment (0/100), shear bands
359 gradually developed at the critical depth as the intrusion arrested and subsequently
360 forms a split tip (Fig. 7D). One of the arms grows larger and later serves as the main
361 conduit for the eruption while the other ceased to be active (Fig. 7D; right column).

362 In all experiments, when the intrusion reaches its critical depth, the observed
363 localized shear bands affecting the overburden generally curve from the intrusion tip to

364 the surface, steepening as they came shallower, and finally intersecting with the surface
365 almost perpendicularly.
366

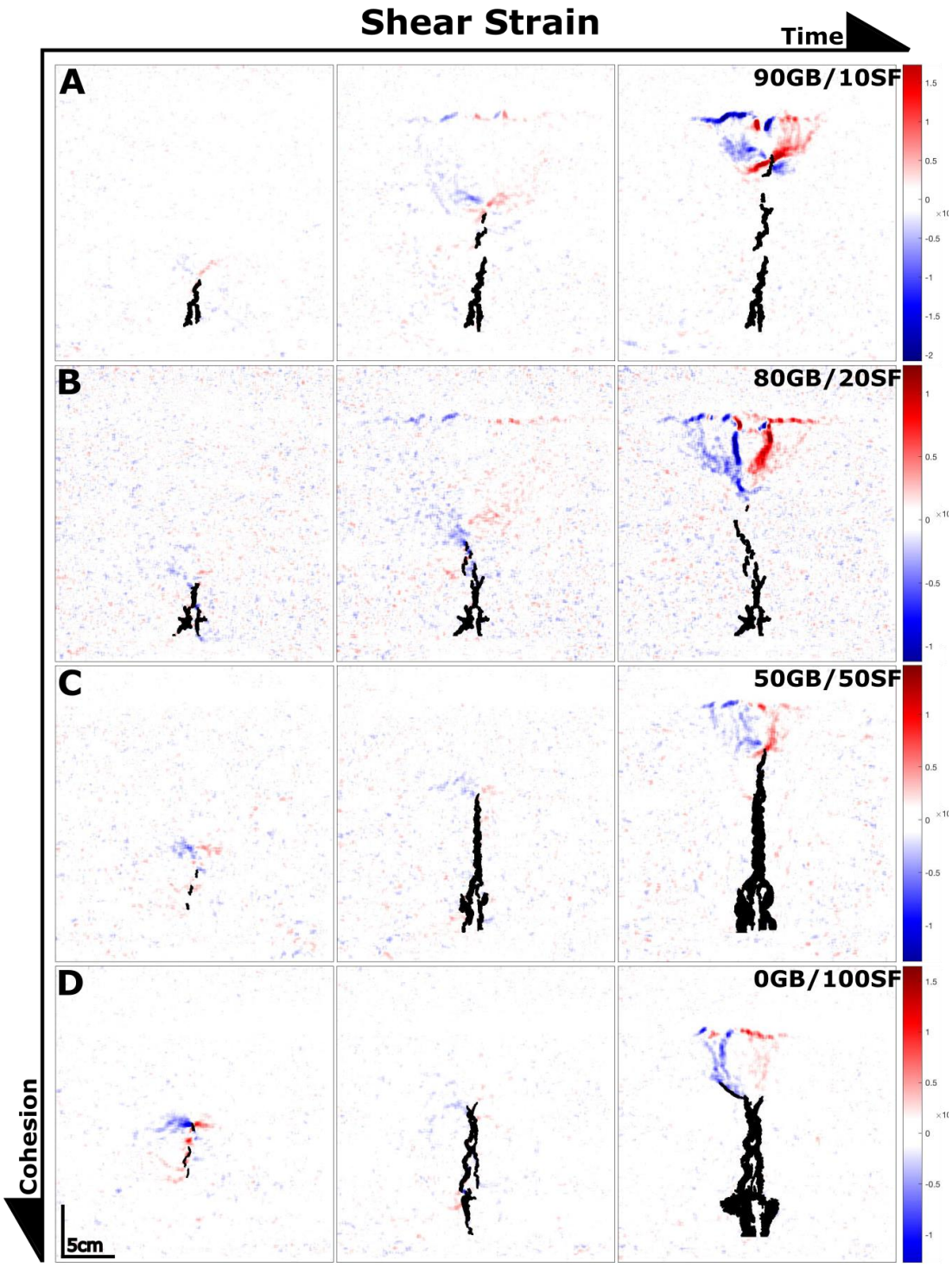

Figure 7. The rows show intrusions (black) into mixes of 90/10 (A), 80/20 (B), 50/50 (C) and 0/100 (D). Columns show experiment photos at an initial, intermediate and late time step. The computed shear strain in A and B extends from the intrusion already at depth until ultimately causing critical failure of the overburden. C & D shows smaller zones of shear associated with the intrusion tip. The

scale has been limited enhance smaller shear strains at depth. Accelerated experiment videos are available in supplemental material S2.

Pressure and Displacement Analysis

The pressure evolution curves for the low cohesion and high cohesion experiments show drastically distinct behaviors. In the low lower cohesion experiments, an initial pressure buildup is followed by a gradual pressure decrease until eruption occurs (Fig. 8A, B). In contrast, in the higher cohesion experiments (Fig. 8C, D), an initial rapid pressure build-up is followed by a rapid pressure drop. After this initial pressure peak, pressure gradually increases until a second pressure drop occurs just before eruption.

In one of the 80/20 host experiments, a very small pressure drop occurred after the initial pressure build-up, while the early stage intrusion displayed sheet intrusion properties, similar to the high cohesion experiments. One of the 90/10 host experiments also displayed a late-stage pressure drop prior to eruption (available in supplemental material S2).

The initial pressure peak appears to anticorrelate with cohesion, as initial pressure peak in the lower cohesion experiments are higher ($3\text{-}4\times10^4$ Pa) than in the higher cohesion experiments ($1.5\text{-}2.5\times10^4$ Pa; Fig. 8). Admittedly, the lower cohesion hosts exert a higher lithostatic stress but even when accounting for this difference the pressure and cohesion anticorrelation remains. In all experiments, the pressure after eruption ranges between $0.9 – 1.5 \times10^4$ Pa with the low cohesion host experiments being at the higher end of this range.

To interpret the pressure evolution curves in terms of intrusion dynamics, we attempt to correlate the evolution of pressure with the deformational evolution of the host. To do so, we filter the horizontal and vertical displacement maps from noise and compute the average incremental displacements throughout the experiment: U_{xR} for horizontal displacements to the right, U_{xL} for horizontal displacements to the left and U_y for vertical displacements. This calculation provides a combined measure of the magnitude of displacement and of the displaced area (Fig. 8). In the lowest cohesion experiment (Fig. 8A), the average horizontal displacements U_{xR} and U_{xL} initiate once the initial pressure peak has been reached. Then U_{xR} and U_{xL} reach a plateau between ~750 s, when stable vertical propagation initiates, and ~2500 s when the intrusion

reaches the critical depth and failure of the overburden occurs. The average vertical displacement U_y also initiates at an early stage (~500 s), and gradually increases until reaching a constant value at ~2000 s. This increasing stage corresponds to the uplift of a triangular area of the intrusion overburden that transitions into a stable stage due to the narrowing of the uplifting cone counterbalanced by the increased uplift magnitude (Fig. 6A; left and right column).

In the 80/20 host (Fig. 8B), U_{xR} and U_{xL} gradually increase between ~300 s and ~1500 s, while the sheet intrusion lengthens; subsequently, U_{xR} and U_{xL} reach a short plateau before decreasing in value from ~2300 s, before eruption. The evolution of U_y displays a similar trend to the experiment using a 90/10 mix. The main difference being that U_y does not reach a plateau and instead suddenly decreases after reaching its maximum value at ~2300 s (Fig. 8A). We attribute this shortened plateau to the increased cohesion of the host allowing localized failure to occur and create pathways ahead of the intrusion.

In both experiments with higher cohesion mixes, we observe a gradual increase of U_{xR} and U_{xL} with time, and negligible U_y during most of the experiment duration (Fig. 8C, D). Suddenly at ~4000-4500 s, U_{xR} and U_{xL} strongly decrease and U_y reaches a sharp peak; note that this coincides with the pressure drop, and we interpret this behavior as the result of failure of the overburden ahead of the intrusion. Note that the values of U_{xL} are higher than the values of U_{xR}. This suggests asymmetrical opening of the intrusion, but this may also be an artifact due to syrup flow along the glass. The latter is especially present in the experiments in 100% silica flour during the arrest phase of the dyke (see Fig. 3D).

In all experiments, the average displacements started growing only after the pressure reached its peak (Fig. 8). For higher cohesion experiments, this seems to coincide with the end of the initial pressure peak, i.e. after the first pressure drop. The second pressure drop in the higher cohesion experiments is associated with substantial uplift, after which most displacements cease.

To complement the average displacements, we extract the maximum incremental horizontal and vertical displacements (Fig. 8; central and right columns). All experiments show initial large horizontal displacements, as the intrusion initiates, followed by a decrease (Fig. 8). In the experiments with 90/10 and 80/20 hosts, the maximum incremental displacements remain constant, until they increase as the

intrusion approaches the surface (Fig. 8A, B). In both low cohesion experiments, the maximum vertical uplift gradually accelerates as the intrusion rises through the model; the maximum vertical uplift then suddenly decreases after failure of the overburden occurs shortly before eruption.

In the 50/50 experiment, the maximum horizontal displacements exhibit a first peak at ~1000 s, followed by a low at ~1500 s, then followed by rapid increase leading to a stable value during vertical ascent of the intrusion (Fig. 8C). We also note that the left side is constantly opening more than the right side. Failure of the overburden is associated with large horizontal maximum displacements (Fig 8C; central column). Uplift throughout the experiment is generally low during most of the experiments except for isolated timesteps. It accelerates rapidly when the intrusion approaches the free surface and the overburden fails ahead of the intrusion (Fig 8C; right column).

The highest cohesion experiment, 0/100, displays high initial maximum horizontal displacements at ~1500 s, followed by a gradually decreasing trend as the intrusion propagates (Fig. 8D; central column). In similarity with the 50/50 experiment, asymmetrical opening is evident in the average displacement, where the left side is opening significantly more than the right side. However, the large difference in average displacement is not echoed in the maximum displacement. This suggests that the average displacement calculation may have been influenced by flow parallel to the glass. Maximum uplift is low during most of the experiment, except for patches occurring in the early stages of the experiment, whereas the major uplifts occurred only in the late stage (Fig. 8D; right column). Here, critical failure of the overburden occurs creating open fractures acting as fluid pathways to the surface (Fig. 3). We associate the final uplift and horizontal displacement peaks to the uplifting of a block at the surface (Fig. 3).

Interpretation: emplacement mechanisms

Our results suggest that host cohesion plays a significant effect on the emplacement mechanics of the intrusion of a viscous fluid. At least two significantly differing emplacement mechanisms can be identified for the high and low cohesion hosts. In the following section we will interpret each set of experiments

Emplacement mechanism in the 50GB/50SF high cohesion experiments

For 50GB/50SF experiments, prominent planar sheet intrusions formed (Fig. 3C). The intrusion tip was generally narrow and sharp. During intrusion at depth, i.e. below the *critical depth*, there was very little or no uplift (Fig. 6C). Concurrently, a horizontal displacement halo could be observed indicating opening and minor compaction of the material along the fracture (Fig. 5C). The opening of the fracture appears to be slightly asymmetrical with one side opening more than the other (Fig. 8 C). The zone around and ahead of the fracture tip displays intermittent shear bands suggesting that the vertical sheet intrusions are propagating through both opening of the fracture and pushing ahead of the fracture tip (Fig. 7C). Pressure monitoring shows that the higher cohesion experiments (both 50/50 and 0/100) after the initial pressure peak, exhibited a significant pressure drop and a subsequent gradual pressure increase during vertical propagation. The initial pressure peak and subsequent drop, exhibit similar pressure behavior to that seen of hydraulic fractures [cf. *Murdoch*, 2002]. Finally, the intrusion of the sheet occurred step-wise, by arrested episodes of widening followed by transient bursts of propagation as seen in the propagation velocity (Fig. 4C). Some of these observation match well with that of hydraulic fractures such as the pressure curve and the sharp and narrow shape of the intrusion. However, the shear bands ahead of the tip and minor compaction of the host indicate non negligible plastic deformation playing an important role in the emplacement mechanics. Thus, we conclude that the syrup in the 50GB/50SF experiment was emplaced through a combined mechanism of dyke opening and widening along the entire walls and pushing ahead at the tip.

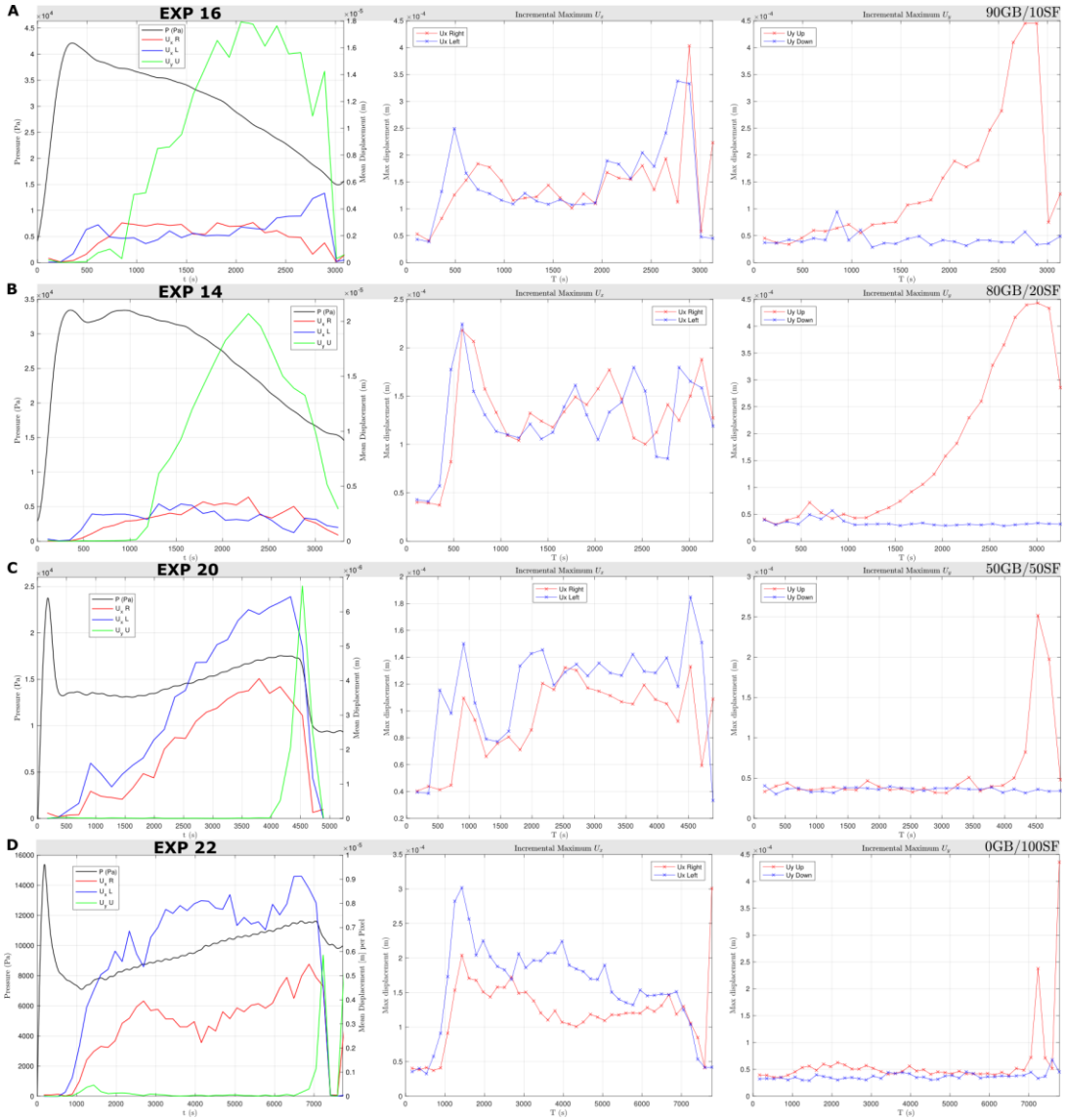

Figure 8. *Left column* Pressure and average displacement plots for 90/10 (A), 80/20 (B), 50/50 (C) and 0/100 (D). The black line shows pressure associated with the left axis. Blue and red lines are left and right average displacements, respectively and green shows upward average displacement associated with the right axis. Plots of additional experiments are available in the supplemental material S2. *Center and right column* Incremental maximum displacements in the left column for left (blue) and right (red) and in the right column for displacements upward (red) and downward (blue). Plots of additional experiments are available in the supplemental material S2.

487

488

489 *Emplacement mechanism in the 0GB/100SF high cohesion experiments*

490 The data monitored of the highest cohesion experiment (0/100) match well with that of
491 the 50/50 experiment except that it showed signification signs of compaction during
492 propagation at depth. All other experiments showed a quasi-constant maximum lateral

493 opening of the host during vertical propagation (Fig. 8 middle column). This was not
494 the case for the 100% silica flour that showed an initial large maximum opening that
495 gradually decreased (Fig. 8D middle column). The tip of the intrusion approached a
496 standstill at the *critical depth* during which the intrusion dilated and opened until finally
497 failing the overburden (Fig 4). It seems plausible therefore that compaction of the host
498 played a role in temporarily arresting or stalling the intrusion in favor of dilation rather
499 than upward propagation increasing the overall duration of the experiment. The role of
500 compaction or an effective strain hardening in association with magma emplacement
501 has not been greatly studied but has been proposed to play a non-significant role
502 [*Summer and Ayalon*, 1995; *Schmiedel et al.*, 2017b]. Similarly to the 50GB/50SF
503 experiments, the syrup was emplaced through a combined mechanism of dyke opening
504 and widening along the entire walls and pushing ahead at the tip. In addition, the dyke
505 widening was accommodated by inelastic compaction of the host.
506
507 *Emplacement mechanism in the 90GB/10SF low cohesion experiments*
508 The discontinuous nature of the intrusion in the 90GB/10SF experiment, visible in the
509 experiment photographs (Fig. 3A), suggest a complex intrusion shape in the third
510 dimension, i.e. a finger shape. This is confirmed when excavating the intrusion, which
511 exhibits a finger-like tubular shape. The time series of vertical deformation show that
512 the intrusion is associated with significant uplift already when the intrusion was at depth
513 (Fig. 6A). The uplift increases throughout the experiment until the intrusion reaches the
514 c*ritical depth,* where the overburden fails. The in-plane horizontal deformation
515 demonstrates that in low cohesion hosts, deformation is concentrated to the tip region
516 during propagation at depth (Fig. 5A). The concentration of horizontal deformation to
517 the tip is drastically different form that observed in the two higher cohesion experiments
518 described above. When the *critical depth* is reached, horizontal deformation extends
519 from the intrusion tip up until the surface. The analysis of shear deformation in the host
520 revealed larger reverse shear zones ahead of the intrusion tip compared to high cohesion
521 experiments (Fig. 7). This indicates that there is a significant component of pushing of
522 the fluid ahead of the path in which it is propagating. However, the shear bands ahead
523 of the tip become weaknesses that may act as precursors for the subsequent propagation
524 of the intrusion [*Pollard*, 1973; *Haug et al.*, 2017; *Schmiedel et al.*, 2019]. This may
525 explain the undulating nature of the intrusion. The pressure readings exhibit a very

different behavior than what was seen for high cohesion experiments (Fig. 8), suggesting a drastically different emplacement dynamics than hydraulic fracturing. The propagation velocity also indicates the low cohesion experiments to propagate in bursts. However, due to the aforementioned 3D-nature of the intrusion shape we must caution against interpreting this as definite evidence. I.e., it is not sure that we are at all times properly tracking the intrusion tip in these experiments and therefore we must consider this observation to be inconclusive. We conclude from these observations that the finger-shaped intrusions in the 90GB/10SF experiments result from a "viscous indenter" mechanism, i.e. the viscous magma makes its own space by pushing the host ahead, which fails dominantly in shear.

Emplacement mechanism in the 80GB/20SF low cohesion experiments

The host material in the 80GB/20SF experiment has a slightly larger cohesion than that in the 90GB/10SF experiment. This experiment overall exhibits many of the same characteristics as the previous low cohesion experiment (Figs. 3, 5-8). However, due to the higher cohesion the intrusion initially formed a sheet intrusion at the base of the model and transitions into a finger shaped intrusion (Fig. 3B). Fig. 5B Left shows this transition occurring with a horizontal displacement halo occurring simultaneously as there are lobes of horizontal deformation focused to the tip. Subsequent timesteps, below the *critical depth*, only show horizontal deformation focused to the intrusion tip. Similarly, Fig. 8B Left displays a brief low amplitude pressure drop followed by a transient pressure increase similarly to that of the higher cohesion experiments but then transitions into the linearly decreasing pressure displayed in the 90/10 experiment. We believe this to be associated with the sheet intrusion at the base of the intrusion and the transitions into a finger intrusion associated with pressure dropping as it propagates towards the surface. We therefore consider the 80/20 experiment to be a hybrid intrusion and an interesting look into the transition from one emplacement mechanism to another.

Emplacement mechanisms above the critical depth

In all experiments, a clear transition happens at a few centimeters depth, referred to as the *critical depth*. Here, rapid uplift occurs associated with failure of the overburden and a change in the emplacement mechanism for both lower and higher cohesion

559 experiments. *Abdelmalak et al.* [2012] and *Poppe et al.* [2019], who similarly observed
560 this shallow mechanism, showed that when the dyke tip is shallow enough, it is more
561 favorable to lift up the overburden, which entire fails along shear bands from the dyke
562 tip to the surface. This is supported by the sudden pressure drop happening when the
563 dyke lifts up the overburden at the critical depth. This mechanism illustrates how the
564 damage created ahead of the intrusion has the potential to act as weaknesses and
565 mechanical precursors for the intrusion to utilize and intrude into [e.g. *Haug et al.*,
566 2017; *Schmiedel et al.*, 2019].
567
568 *Summary - Emplacement mechanisms below the critical depth*
569 Below the critical depth, we document two types of emplacement mechanics depending
570 on host cohesion. (1) For low cohesion hosts, a finger-shaped intrusion formed as a
571 viscous indenter. In this mechanism, the intrusion tip pushes its host ahead, and the
572 opening of the intrusion only focuses near the tip. (2) For high cohesion hosts, a sheet
573 intrusion formed as a fracture. In this mechanism, the intrusion thickens by opening
574 along its entire length, and the tip propagates by intermittent local opening and pushing
575 of the host with a horizontal deformation halo surrounding the entire opening fracture
576 (Fig. 9). These two emplacement mechanisms exhibited distinctly different pressure
577 behavior, illustrating distinct emplacement dynamics. Both emplacement mechanisms
578 were associate with shear bands. The shear bands were larger in areal extent as well as
579 magnitude for the lower cohesion experiments. The shear bands were intermittent in
580 high cohesion hosts and associated with upward propagation of the intrusion while they
581 appeared more continuous for the lower cohesion experiments. Our experiments
582 evidence the great role of host rock cohesion on the dynamics of emplacement of
583 viscous liquids in Mohr-Coulomb hosts. Especially, our experiments show that sheets
584 intrusions are favored in high-cohesion hosts whereas finger-shaped intrusions are
585 favored in low-cohesion hosts.
586

587 # Discussion

588

589 *Experimental constraints*
590 The experiments presented in this article use model host rocks made of compacted
591 cohesive mixes of silica flour and glass beads. Such materials fail according to Mohr-

Coulomb criterion similar to rocks found in the shallow crust [*Jaeger et al.*, 2009]. Due to its cohesiveness, the 100% silica flour withstands non-negligible elastic stresses, as it sustains vertical walls under the load of its own weight [*Abdelmalak et al.*, 2016; *Guldstrand et al.*, 2017]. Conversely, pure glass beads collapse under their own weight and are close to cohesionless [*Galland et al.*, 2006; *Abdelmalak et al.*, 2016; *Schmiedel et al.*, 2017b]. In addition, the 100% silica flour exhibits a higher friction coefficient than the 100% glass beads. Therefore, we can fine-tune and study the effect of cohesion and friction on intrusion experiments by using mixes of these two materials [*Abdelmalak et al.*, 2016; *Schmiedel et al.*, 2017b]. The presented experiments are the first ones that investigate systematically the effect of rock cohesion and friction on the emplacement of dykes.

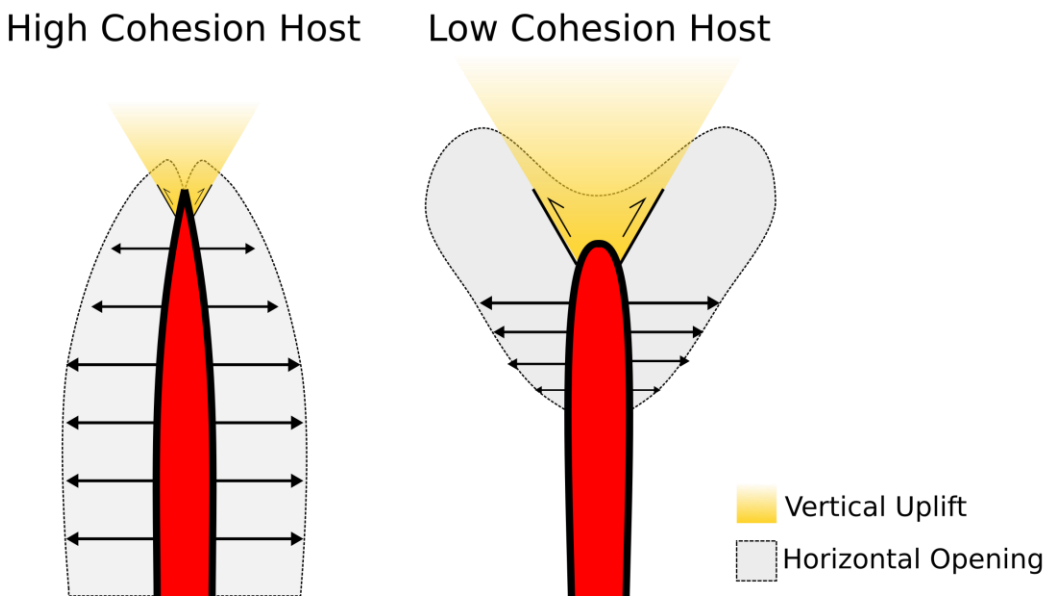

Figure 9. Interpretative sketch of the emplacement mechanics at play in high cohesion experiments (right) and low cohesion experiments (left). Shaded grey area denotes areas of horizontal deformation.

However, these materials and the experiment setup include some limitations. First, our experiments are homogeneous, i.e. without layering. Second, they assume lithostatic stress and do not account for the influence of tectonic stresses or stresses dues to topography. Additionally, the use of granular Mohr-Coulomb materials do not allow for quantifying and extracting the elastic and plastic deformation separately [*Guldstrand et al.*, 2017].

The 2D Hele-Shaw cell ideally intends to simulate 2D processes in plain strain configuration, however in practice this is not the case. First, the friction of the granular materials along the glass walls trigger 3D stress distributions within the models. Second, in the low cohesion experiments, the intrusions cannot be considered strictly 2D as they consist of finger intrusions that appear disconnected on the observation plane, but connected in the third dimension. Nevertheless, the displacement maps and videos (supplemental material S2) show that the deformation monitored correlates well with the extracted intrusion from the experiment photos such that we are confident that we are tracking relevant deformation to the respective intrusions.

The tracking of the intrusion tip revealed significant advances in propagation to occur in bursts. This was more evident for lower cohesion hosts than in higher cohesion hosts, such that the average propagation velocity was higher in hosts of lower cohesions and lower in hosts of higher cohesions. Admittedly there are limitations in tracking the tip in the initial and final times of the experiments and in lower cohesion experiments as we may have more 3D effects in these experiments where we cannot track the tip of the intrusion. This means that we cannot strictly consider the observed burst dynamics to be strictly linked to emplacement mechanism for low cohesion experiments.

One may attribute the differing sheet and finger intrusion emplacement mechanisms and pressure readings to buoyancy. By just comparing densities, the syrup is indeed positively buoyant compared to the low cohesion glass beads and negatively buoyant compared to the high cohesion silica flour (see Table 1). However, we performed further analysis that show that the pressure within the syrup, when corrected for stresses due to viscous pipe flow and buoyancy, still remain significantly higher than the lithostatic stress for a given depth for all but one of the experiments into 100% silica flour (cf. supplemental material S3). This was calculated by taking the difference between the pressure readings and the hydrostatic stress of the fluid at a given tip depth and the viscous stress due to pipe flow when entering the setup (calculated through the Hagen-Poiseuille equation). This was compared to the lithostatic stress and the expected stress perpendicular to the dyke at a given depth. No interaction was observed between these pressure curves in all but one experiment (100% silica flour). In addition, the differences between the high-cohesion and low-cohesion experiments were noticeable already in the very early phases of the experiments, i.e. when the intrusions

were small and so the buoyancy effects negligible. We infer that in all experiments the effects of buoyancy were secondary and cannot explain the differences of pressure evolutions in the experiments.

The role of plastic deformation during magma emplacement in the brittle crust

Our experiments highlight that small-scale (shear bands) and large-scale (compaction) plastic deformation can greatly control the propagation of sheet intrusions. In detail, our experiments show how local shear damage controls locally the propagation of the intrusion tips. Our laboratory results corroborate well (1) field observations of igneous fingers emplaced in low-strength rock [e.g. shale *Pollard et al.*, 1975; *Spacapan et al.*, 2017; *Galland et al.*, 2019] and elasto-plastic numerical models [*Haug et al.*, 2017; *Haug et al.*, 2018; *Souche et al.*, 2019], which evidence how local plastic damage at the tip of propagating intrusions trigger weaknesses favorable to the subsequent propagation of the magma. Our experimental results provide a viable alternative mechanism to the widely established models of sheet intrusion emplacement, which assume intrusion propagation by tensile failure through a purely elastic host. Further research is now necessary to constrain under which geological conditions elasticity- or plasticity-dominated emplacement of igneous sheet intrusions occur.

Sheets versus fingers - Implications for dike and sill emplacement in the brittle crust

Our experiments evidence two drastically distinct emplacement mechanisms of a viscous fluid in Mohr-Coulomb hosts of varying cohesions and friction angles, and the resulting intrusions exhibit different shapes, i.e. continuous sheets with relatively sharp tips in high-cohesion hosts versus aligned fingers in low cohesion hosts (Fig. 3). The modes of deformation of the host accommodating the emplacement of the viscous liquid also differ, with significantly more shear damage and failure in the low-cohesion hosts. Such difference has been proposed by *Galland et al.* [2014] on the basis of a scaling argument, and documented by *Poppe et al.* [2019].

The scaling argument of *Galland et al.* [2014], however, does not only involve the host cohesion, but it considers the mechanical coupling between the viscous stresses in the flowing liquid and the strength (i.e. cohesion) of the host rock. This scaling implies that when the viscous stresses dominate over the cohesive forces, the host rock deforms dominantly by shear failure. Our experiments corroborate well this

theoretical prediction, in agreement with the experiments of *Poppe et al.* [2019]. Our experiments show that not only the deformation mechanisms of the host differ, but also the emplacement dynamics of the liquid and the resulting intrusion shape.

Applied to geological systems, it predicts that fingers are expected to form preferably when the magma is highly viscous (e.g. andesitic to rhyolitic magmas) and/or when the host rock exhibits low cohesion (e.g. volcanic tuff, shale, poorly consolidated sandstones). Geological observations corroborate well this prediction. Igneous fingers observed in nature are often made of felsic magmas (andesitic to rhyolitic) [e.g. *Pollard et al.*, 1975; *Spacapan et al.*, 2017; *Galland et al.*, 2019] or were emplaced in very low strength host rock [*Duffield et al.*, 1986; *Schofield et al.*, 2012]. Conversely, clear igneous sheets are common to mafic, i.e. low viscosity, magmas emplaced in relatively high cohesion host rock [e.g. *Gudmundsson*, 2020; *Poppe et al.*, 2020]. Therefore, we expect that fingers form preferably at felsic volcanoes and/or in sedimentary basin settings whereas sheets form preferably at mafic volcanoes.

The overall shapes of the model intrusions differ: in the high-cohesion experiments, the sheets are continuous with sharp tips, whereas in low cohesion experiments the intrusions are made or aligned fingers with more blunt tips. Nevertheless, outcrop observations rarely provide exposures of entire intrusions, so that only short segments are observable. For instance, if only a short segment of a finger, without the tip, in our low-cohesion experiments was observable, one could easily extrapolate that the overall intrusion is a sheet. Thus, the overall inferred shape and emplacement mechanism of the observed intrusion would be incorrect. A field example illustrates this discussion point. The kilometer-scale outcrop studied by [*Galland et al.*, 2019] exhibits an intrusion with an overall shape of a sill, however, it is made of a string of fingers. This interpretation was only possible because (1) the outcrop was large enough to display the gaps between the fingers and (2) the blunt tips and the surrounding structures in the host were exposed. If only the central part of a finger, with parallel top and bottom contacts, were exposed, or if the outcrop were discontinuous and did not expose the gaps between the fingers, one would naturally interpret this intrusion as being a sheet. Therefore, a local sheet shape is not conclusive to interpret the nature and the emplacement mechanism on intrusions. This example shows that intrusion-scale observations in addition to tip observations are necessary to infer the nature and emplacement mechanisms of intrusions in the brittle crust. It implies that

711 numerous dykes and sills have likely been interpreted as sheets, whereas they are strings
712 of fingers, and their emplacement mechanisms are radically different.

713 Host rocks of volcanic plumbing systems in volcanic environments and in
714 sedimentary basins are typically made of layers, the strength of which can vary
715 considerably from competent (e.g., consolidated sandstone or crystalline rock) to
716 weaker rock (e.g. volcanic tuff in volcanic environment of shale in sedimentary basins)
717 [*Ranalli*, 1995; *Galland et al.*, 2018]. In the literature, the effects of the layering on
718 magma emplacement has been addressed through static stress analysis resulting from
719 stiffness contrast between the layers [*Gudmundsson*, 2020]. Yet so far the effect of this
720 strength variation has only just started to be studied [*Vachon and Hieronymus*, 2016;
721 *Haug et al.*, 2017; *Schmiedel et al.*, 2017a; *Souche et al.*, 2019]. Our experimental
722 results suggest that the propagation mechanisms of an intrusion through layered crust
723 may greatly vary from elasticity-dominated to plasticity-dominated depending on the
724 local cohesion of the host rocks it propagates through, such that the propagation
725 mechanism and dynamics may considerably vary from that of a sheet to that of a finger,
726 and *vice versa*. Such variety of propagation mechanisms may explain why igneous sills
727 and fingers tend to concentrate in low-strength host rock such as tuff and shale [e.g.
728 *Rodriguez Monreal et al.*, 2009; *Spacapan et al.*, 2020]. Similarly, recent field studies
729 in the Swedish and Norwegian Caledonides show that the emplacement of dykes can
730 vary laterally and through time as the thermal state of the host vary [*Kjøll et al.*, 2019]:
731 cold hosts behave competent and dykes are emplaced similarly to our high-cohesion
732 experiments, but when the host rock gets hotter due to geodynamic processes, it can
733 behave weak and dykes are emplaced similarly to our low-cohesion experiments. The
734 close similarities between our experimental results and field observations strongly
735 suggest that the lateral and temporal variations of inelastic properties of crustal rocks
736 play a major role on the emplacement of igneous sheet intrusions.

737 Dyke arrest, i.e. the halting of vertical propagation of sheet intrusions, has often been
738 attributed to the interaction with a more competent layer [*Rivalta et al.*, 2005;
739 *Gudmundsson*, 2020], a weak interface [*Kavanagh et al.*, 2015; *Kavanagh et al.*, 2017]
740 or due to reaching its neutral level of buoyancy [*Hogan et al.*, 1998; *Taisne et al.*, 2011].
741 However, our experiments show that temporary halting of the model dykes can occur
742 without layering and with constant magma influx. We infer from our experiments that
743 the widening of the model dyke due to host compaction and cohesion may inhibit

744 vertical propagation, as the volume of the incoming magma is accommodated by dyke
745 widening rather than by dyke lengthening.
746
747 *Geophysical and geodetic implications*
748 The host deformation patterns accommodating dike and finger emplacement in our
749 Mohr-Coulomb models do not match those predicted by static linear elastic model (e.g.
750 Okada dislocation model). In all our experiments, only uplift above the propagating
751 intrusions are observed [Figures 6 and 8; cf. *Guldstrand et al.*, 2017]. To date, there is
752 no elastic geodetic model able to calculate only uplifting dome above a sub-vertical
753 intrusion. For example, the elastic Okada model tends to produce two uplifting bulges
754 delineated by a trough above, and aligned with, the orientation of the underlying sheet.
755 However, symmetric and asymmetric doming has frequently been documented in
756 nature [e.g. *Amelung et al.*, 2000; *Wright et al.*, 2006; *Jay et al.*, 2014], and the Okada
757 model fails to interpret such data. Instead, these types of uplift are commonly modelled
758 using inflating point sources or sub-horizontal inflating planar dislocations, despite the
759 evidence of upward magma transport leading to eruption (e.g., Sigmundsson et al.,
760 2010). Our experimental results suggest that surface doming can be interpreted as a
761 result of dike emplacement controlled by the Coulomb properties of the crust. Such
762 interpretation is corroborated by field observations of steeply dipping reverse faults
763 associated with the emplacement of dykes in the shallow part of the crust, even in
764 extensional settings [*Gudmundsson et al.*, 2008]. Therefore, our models show the
765 limitation of the systematic use of elastic geodetic models to interpret geodetic signals
766 monitored at active volcanoes, and strongly suggest that accounting for viscous flow
767 [as already demonstrated by *Marsden et al.*, 2019] and Mohr-Coulomb host rheology
768 are essential to understand magmatic systems and the deformation it produces.
769 Stepwise propagation, as demonstrated in our high cohesion experiments,
770 implies that fast advances of the intrusion tip can happen over short periods of time.
771 However, in between bursts, the tip may also advance smoothly. The burst propagation
772 of the dyke in our experiments are in good agreement with the seismicity monitored
773 during the 2014-2015 Bárðarbunga dyke intrusion, which revealed burst-like
774 propagation [*Ágústsdóttir et al.*, 2016]. In addition, the seismicity at Bárðarbunga was
775 not only active at the dyke tip but also remained active behind the interpreted dyke
776 front. This observation is in good agreement with our high cohesion experiments, which

show that inelastic horizontal deformation affected the host over the entire fracture length, i.e., it is plausible that seismic activity would be active both at the dyke tip and below/behind the tip during intrusion.

Implications for magma emplacement in felsic volcanoes and the formation of cryptodomes

Our experiments aim to study volcanism in which the ratio of viscous stresses to cohesive stresses is non-negligible. This is more likely to be the case in areas with weak crust (such as in sedimentary basins or volcanic environments with pyroclastic deposits) and where there is felsic volcanism (i.e. high viscosity magma) [*Galland et al.*, 2014]. Sheet intrusions, such as dykes, are commonly thought to be associated with low viscosity resulting in thin sheets with sharp tips [e.g. *Poppe et al.*, 2020] however there are observations supporting high viscosity dykes to be more prolific than previously thought [*Fink*, 1985; *Poland et al.*, 2008]. These studies show that these sheet intrusions are generally thicker than their low-viscosity counterparts. This is in agreement with the thicker sheets produced in our experiments compared to gelatine-water models [*Kavanagh et al.*, 2018]. Moreover, we find that as cohesion decreases the sheets gets thinner and finally transitions into a finger-shaped intrusion similar in shape to andesitic sills observed in sedimentary basins [*Spacapan et al.*, 2017; *Galland et al.*, 2019]. The shapes of intrusions and associated strain patterns in our observations match very well with field observations of felsic sills emplaced in low strength/low friction shale. Overall, our experiments suggest that finger-shaped intrusions are likely essential elements of felsic magma transport.

The shallow emplacement of the syrup in our experiments exhibits characteristics of cryptodome emplacement, i.e. largely cylindrical or elongated bodies associated with uplift and planes of shear failure [*Okada et al.*, 1981; *Donnadieu and Merle*, 1998]. The emplacement of cryptodomes is a characteristic of another high-viscosity magma intrusions in the shallowest crust [e.g. *Stewart and McPhie*, 2003; *Burchardt et al.*, 2019]. The localized uplift and associated reverse fault planes in the latest stages of our experiments is in good agreement with uplift and semi-circular locations of seismicity at depth associated with the emplacement of a cryptodome at Usu volcano [*Okada et al.*, 1981; *Tobita et al.*, 2001]. Our experimental setup thus appears as a relevant tool for studying the dynamics of cryptodome emplacement.

Conclusions

In this study, we present quantitative laboratory experiments simulating the intrusion of viscous magma into host rock of varying cohesion, in order to quantify the effects of the Mohr-Coulomb properties of crustal rocks on the emplacement of planar intrusions. The main conclusions are as follows:

1. Continuous sheet intrusions form in high-cohesion hosts, whereas discontinuous finger-shaped intrusions form in low-cohesion hosts.
2. In all experiments, inelastic shear damage with, and uplift of, the host accommodate partly the emplacement of the model magma.
3. Sheet intrusions in high-cohesion hosts grow dominantly by dilation and opening along the entire length of the intrusion. In contrast, finger-shaped intrusions only thicken near the propagating tip of the intrusion.
4. The propagation of the fingers' tips is accommodated by significant shear damage bands, showing that the fingers dominantly propagate by pushing their host rock ahead, in agreement with the so-called *viscous indenter* model. Conversely, shear damage is much less prominent near the tip of sheet intrusions, which dominantly propagate like fractures.
5. In all experiments, when the intrusion tip reached a shallow critical depth, the overburden is pushed upward and fails along shear damage bands, which control the subsequent propagation of the model magma. This shallow emplacement mechanism is likely relevant for revealing the emplacement of cryptodomes in nature.
6. When magma is emplaced in layered host, like in sedimentary basins, it is likely that both emplacement mechanisms successively occur.
7. All in all, our experiments suggest that the Mohr-Coulomb properties of the crust must be systematically accounted in models of planar intrusion emplacement.

Acknowledgements

Guldstrand and Souche's position was funded by the DIPS project (grant no. 240467) from the Norwegian Research Council. Bertelsen's position was funded by the Faculty of Mathematics and Natural Sciences of the University of Oslo. The authors thank

Tobias Schmiedel & Marcel Moura for assistance in determining wetting by performing contact angle measurements. Regis Mourgues is acknowledged for assisting in setting up a guest researcher visit in Le Mans to study their experimental setup. The data presented in this study is available on demand.

References

Abdelmalak, M. M., R. Mourgues, O. Galland, and D. Bureau (2012), Fracture mode analysis and related surface deformation during dyke intrusion: Results from 2D experimental modelling, *Earth Planet. Sci. Lett.*, *359-360*, 93-105.

Abdelmalak, M. M., C. Bulois, R. Mourgues, O. Galland, J. B. Legland, and C. Gruber (2016), Description of new dry granular materials of variable cohesion and friction coefficient: Implications for laboratory modeling of the brittle crust, *Tectonophysics*, *684*, 39-51.

Ágústsdóttir, T., J. Woods, T. Greenfield, R. G. Green, R. S. White, T. Winder, B. Brandsdóttir, S. Steinthórsson, and H. Soosalu (2016), Strike‐slip faulting during the 2014 Bárðarbunga‐Holuhraun dike intrusion, central Iceland, *Geophysical Research Letters*.

Amelung, F., S. Jónsson, H. Zebker, and P. Segall (2000), Widespread uplift and 'trapdoor'faulting on Galapagos volcanoes observed with radar interferometry, *Nature*, *407*(6807), 993-996.

Beckett, F., H. Mader, J. Phillips, A. Rust, and F. Witham (2011), An experimental study of low-Reynolds-number exchange flow of two Newtonian fluids in a vertical pipe, *Journal of Fluid Mechanics*, *682*, 652-670.

Bunger, A. P., and A. R. Cruden (2011), Modeling the growth of laccoliths and large mafic sills: Role of magma body forces, *J. Geophys. Res.*, *116*(B2), B02203.

Burchardt, S., T. Mattsson, J. O. Palma, O. Galland, B. Almqvist, K. Mair, D. A. Jerram, Ø. Hammer, and Y. Sun (2019), Progressive Growth of the Cerro Bayo Cryptodome, Chachahuén Volcano, Argentina—Implications for Viscous Magma Emplacement, *Journal of Geophysical Research: Solid Earth*, *124*(8), 7934-7961.

Delcamp, A., B. v. W. de Vries, M. R. James, L. Gailler, and E. Lebas (2012), Relationships between volcano gravitational spreading and magma intrusion, *Bulletin of Volcanology*, *74*(3), 743-765.

Donnadieu, F., and O. Merle (1998), Experiments on the indentation process during cryptodome intrusions: new insights into Mount St. Helens deformation, *Geology*, *26*(1), 79-82.

Duffield, W. A., C. R. Bacon, and P. T. Delaney (1986), Deformation of poorly consolidated sediment during shallow emplacement of a basalt sill, Coso Range, California, *Bull. Volcanol.*, *48*(2), 97-107.

881 Fink, J. H. (1985), Geometry of silicic dikes beneath the Inyo Domes, California, *Journal of*
882 *Geophysical Research: Solid Earth*, *90*(B13), 11127-11133.
883 Galland, O., and J. Scheibert (2013), Analytical model of surface uplift above axisymmetric flat-
884 lying magma intrusions: Implications for sill emplacement and geodesy, *J.*
885 *Volcanol. Geotherm. Res.*, *253*(0), 114-130.
886 Galland, O., P. R. Cobbold, E. Hallot, J. de Bremond d'Ars, and G. Delavaud (2006), Use of vegetable
887 oil and silica powder for scale modelling of magmatic intrusion in a deforming
888 brittle crust, *Earth Planet. Sci. Lett.*, *243*, 786-804.
889 Galland, O., S. Burchardt, E. Hallot, R. Mourgues, and C. Bulois (2014), Dynamics of dikes versus
890 cone sheets in volcanic systems, *Journal of Geophysical Research: Solid Earth*,
891 2014JB011059.
892 Galland, O., H. S. Bertelsen, F. Guldstrand, L. Girod, R. F. Johannessen, F. Bjugger, S. Burchardt, and
893 K. Mair (2016), Application of open-source photogrammetric software MicMac
894 for monitoring surface deformation in laboratory models, *Journal of Geophysical*
895 *Research: Solid Earth*.
896 Galland, O., J. B. Spacapan, O. Rabbel, K. Mair, F. G. Soto, T. Eiken, M. Schiuma, and H. A. Leanza
897 (2019), Structure, emplacement mechanism and magma-flow significance of
898 igneous fingers – Implications for sill emplacement in sedimentary basins, *J.*
899 *Struct. Geol.*
900 Galland, O., et al. (2018), Storage and transport of magma in the layered crust-Formation of sills
901 and related flat-lying intrusions, in *Volcanic and Igneous Plumbing Systems*,
902 edited by S. Burchardt, pp. 111-136, Elsevier.
903 Gudmundsson, A. (2020), *Volcanotectonics: Understanding the Structure, Deformation and*
904 *Dynamics of Volcanoes*, Cambridge University Press, Cambridge.
905 Gudmundsson, A., N. Friese, I. Galindo, and S. L. Philipp (2008), Dike-induced reverse faulting in a
906 graben, *Geology*, *36*(2), 123.
907 Guldstrand, F., S. Burchardt, E. Hallot, and O. Galland (2017), Dynamics of Surface Deformation
908 Induced by Dikes and Cone Sheets in a Cohesive Coulomb Brittle Crust, *Journal*
909 *of Geophysical Research: Solid Earth*, *122*(10), 8511-8524.
910 Guldstrand, F., O. Galland, E. Hallot, and S. Burchardt (2018), Experimental Constraints on
911 Forecasting the Location of Volcanic Eruptions from Pre-eruptive Surface
912 Deformation, *Frontiers in Earth Science*, *6*(7).
913 Halls, H. C., and W. F. Fahrig (Eds.) (1987), *Mafic dyke swarms*, 503 pp., Toronto, Canada.
914 Haug, Ø. T., O. Galland, P. Souloumiac, A. Souche, F. Guldstrand, and T. Schmiedel (2017), Inelastic
915 damage as a mechanical precursor for the emplacement of saucer-shaped
916 intrusions, *Geology*, *45*(12), 1099-1102.
917 Haug, Ø. T., O. Galland, P. Souloumiac, A. Souche, F. Guldstrand, T. Schmiedel, and B. Maillot
918 (2018), Shear versus tensile failure mechanisms induced by sill intrusions --
919 Implications for emplacement of conical and saucer-shaped intrusions, *Journal*
920 *of Geophysical Research: Solid Earth*, *123*, 3430-3449.

921 Hogan, J. P., J. D. Price, and M. C. Gilbert (1998), Magma traps and driving pressure: consequences
922 for pluton shape and emplacement in an extensional regime, *J. Struct. Geol.*,
923 *20*(9-10), 1155-1168.
924 Jaeger, J. C., N. G. Cook, and R. Zimmerman (2009), *Fundamentals of rock mechanics*, John Wiley &
925 Sons.
926 Jay, J., F. Costa, M. Pritchard, L. Lara, B. Singer, and J. Herrin (2014), Locating magma reservoirs
927 using InSAR and petrology before and during the 2011–2012 Cordón Caulle
928 silicic eruption, *Earth and Planetary Science Letters*, *395*, 254-266.
929 Kavanagh, J. L., D. Boutelier, and A. R. Cruden (2015), The mechanics of sill inception, propagation
930 and growth: Experimental evidence for rapid reduction in magmatic
931 overpressure, *Earth Planet. Sci. Lett.*, *421*(0), 117-128.
932 Kavanagh, J. L., B. D. Rogers, D. Boutelier, and A. R. Cruden (2017), Controls on sill and dyke-sill
933 hybrid geometry and propagation in the crust: The role of fracture toughness,
934 *Tectonophysics*, *698*, 109-120.
935 Kavanagh, J. L., A. J. Burns, S. Hilmi Hazim, E. P. Wood, S. A. Martin, S. Hignett, and D. J. C. Dennis
936 (2018), Challenging dyke ascent models using novel laboratory experiments:
937 Implications for reinterpreting evidence of magma ascent and volcanism, *J.*
938 *Volcanol. Geotherm. Res.*, *354*, 87-101.
939 Kjøll, H. J., O. Galland, L. Labrousse, and T. B. Andersen (2019), Emplacement mechanisms of a
940 dyke swarm across the brittle-ductile transition and the geodynamic
941 implications for magma-rich margins, *Earth and Planetary Science Letters*, *518*,
942 223-235.
943 Llewellin, E., H. Mader, and S. Wilson (2002), The rheology of a bubbly liquid, paper presented at
944 Proceedings of the Royal Society of London A: Mathematical, Physical and
945 Engineering Sciences, The Royal Society.
946 Magee, C., et al. (2016), Lateral magma flow in mafic sill complexes, *Geosphere*, *12*(3), 809-841.
947 Marsden, L. H., J. W. Neuberg, M. E. Thomas, P. A. Mothes, and M. C. Ruiz (2019), Combining
948 Magma Flow and Deformation Modeling to Explain Observed Changes in Tilt,
949 *Frontiers in Earth Science*, *7*, 219.
950 Mart, Y., and O. Dauteuil (2000), Analogue experiments of propagation of oblique rifts,
951 *Tectonophysics*, *316*(1-2), 121-132.
952 Mathieu, L., B. v. W. de Vries, E. P. Holohan, and V. R. Troll (2008), Dykes, cups, saucers and sills:
953 Analogue experiments on magma intrusion into brittle rocks, *Earth and*
954 *Planetary Science Letters*, *271*(1), 1-13.
955 Murdoch, L. C. (2002), Mechanical analysis of idealized shallow hydraulic fracture, *Journal of*
956 *Geotechnical and Geoenvironmental Engineering*, *128*(6), 488-495.
957 Okada, H., H. Watanabe, H. Yamashita, and I. Yokoyama (1981), Seismological significance of the
958 1977–1978 eruptions and the magma intrusion process of Usu volcano,
959 Hokkaido, *Journal of volcanology and geothermal research*, *9*(4), 311-334.

960 Poland, M. P., W. P. Moats, and J. H. Fink (2008), A model for radial dike emplacement in
961 composite cones based on observations from Summer Coon volcano, Colorado,
962 USA, *Bulletin of Volcanology*, *70*(7), 861-875.
963 Pollard, D. D. (1973), Derivation and evaluation of a mechanical model for sheet intrusions,
964 *Tectonophysics*, *19*(3), 233-269.
965 Pollard, D. D. (1987), Elementary fracture mechanics applied to the structural interpretation of
966 dikes, in *Mafic dyke swarms*, edited by H. C. Halls and W. F. Fahrig, pp. 5-24, Geol.
967 Assoc. Canada Spec. Pap.
968 Pollard, D. D., O. H. Muller, and D. R. Dockstader (1975), The Form and Growth of Fingered Sheet
969 Intrusions, *Geol. Soc. Am. Bull.*, *86*(3), 351-363.
970 Poppe, S., O. Galland, N. J. de Winter, S. Goderis, P. Claeys, V. Debaille, P. Boulvais, and M. Kervyn
971 (2020), Structural and Geochemical Interactions Between Magma and
972 Sedimentary Host Rock: The Hovedøya Case, Oslo Rift, Norway, *G3*, *21*(3),
973 e2019GC008685.
974 Poppe, S., et al. (2019), An inside perspective on magma intrusion: quantifying 3D displacement
975 and strain in laboratory experiments by dynamic X-Ray computed tomography,
976 *Frontiers in Earth Science*, *7*.
977 Rabbel, O., O. Galland, K. Mair, I. Lecomte, K. Senger, J. B. Spacapan, and R. Manceda (2018), From
978 field analogues to realistic seismic modelling: a case study of an oil-producing
979 andesitic sill complex in the Neuquén Basin, Argentina, *Journal of the Geological*
980 *Society*, jgs2017-2116.
981 Ranalli, G. (1995), *Rheology of the Earth*, Springer Science & Business Media.
982 Rivalta, E., M. Böttinger, and T. Dahm (2005), Buoyancy-driven fracture ascent: Experiments in
983 layered gelatine, *J. Volcanol. Geotherm. Res.*, *144*, 273-285.
984 Rivalta, E., B. Taisne, A. P. Bunger, and R. F. Katz (2015), A review of mechanical models of dike
985 propagation: Schools of thought, results and future directions, *Tectonophysics*,
986 *638*, 1-42.
987 Rodriguez Monreal, F., H. J. Villar, R. Baudino, D. Delpino, and S. Zencich (2009), Modeling an
988 atypical petroleum system: A case study of hydrocarbon generation, migration
989 and accumulation related to igneous intrusions in the Neuquén Basin, Argentina,
990 *Mar. Pet. Geol.*, *26*(4), 590-605.
991 Rosu, A.-M., M. Pierrot-Deseilligny, A. Delorme, R. Binet, and Y. Klinger (2015), Measurement of
992 ground displacement from optical satellite image correlation using the free
993 open-source software MicMac, *ISPRS J. Photogram. Rem. Sens.*, *100*(0), 48-59.
994 Rupnik, E., M. Daakir, and M. Pierrot Deseilligny (2017), MicMac – a free, open-source solution for
995 photogrammetry, *Open Geospatial Data, Software and Standards*, *2*(1), 14.
996 Schmiedel, T., O. Galland, and C. Breitkreuz (2017a), Dynamics of sill and laccolith emplacement
997 in the brittle crust: role of host rock strength and deformation mode, *Journal of*
998 *Geophysical Research: Solid Earth*, *122*(11), 8625-9484.

Schmiedel, T., O. Galland, Ø. T. Haug, G. Dumazer, and C. Breitkreuz (2019), Coulomb failure of Earth's brittle crust controls growth, emplacement and shapes of igneous sills, saucer-shaped sills and laccoliths, *Earth Planet. Sci. Lett.*, *510*, 161-172.

Schmiedel, T., S. Kjoberg, S. Planke, C. Magee, O. Galland, N. Schofield, C. A.-L. Jackson, and D. A. Jerram (2017b), Mechanisms of overburden deformation associated with the emplacement of the Tulipan sill, mid-Norwegian margin, *Interpretation*, *5*(3), SK23-SK38.

Schofield, N., D. J. Brown, C. Magee, and C. T. Stevenson (2012), Sill morphology and comparison of brittle and non-brittle emplacement mechanisms, *J. Geol. Soc. London*, *169*(2), 127-141.

Senger, K., J. Millett, S. Planke, K. Ogata, C. H. Eide, M. Festøy, O. Galland, and D. A. Jerram (2017), Effects of igneous intrusions on the petroleum system: a review, *First Break*, *35*(6), 47-56.

Souche, A., O. Galland, Ø. T. Haug, and M. Dabrowski (2019), Impact of host rock heterogeneity on failure around pressurized conduits: Implications for finger-shaped magmatic intrusions, *Tectonophysics*, *765*, 52-63.

Spacapan, J. B., O. Galland, H. A. Leanza, and S. Planke (2017), Igneous sill and finger emplacement mechanism in shale-dominated formations: a field study at Cuesta del Chihuido, Neuquén Basin, Argentina, *J. Geol. Soc. London*, *174*(3), 422-433.

Spacapan, J. B., A. D'Odorico, O. Palma, O. Galland, E. Rojas Vera, R. Ruiz, H. A. Leanza, A. Medialdea, and R. Manceda (2020), Igneous petroleum systems in the Malargüe fold and thrust belt, Río Grande Valley area, Neuquén Basin, Argentina, *Mar. Pet. Geol.*, *111*, 309-331.

Stewart, A. L., and J. McPhie (2003), Internal structure and emplacement of an Upper Pliocene dacite cryptodome, Milos Island, Greece, *Journal of Volcanology and Geothermal Research*, *124*(1-2), 129-148.

Summer, N. S., and A. Ayalon (1995), Dike intrusion into unconsolidated sandstone and the development of quartzite contact zones, *Journal of Structural Geology*, *17*(7), 997-1010.

Taisne, B., S. Tait, and C. Jaupart (2011), Conditions for the arrest of a vertical propagating dyke, *Bulletin of Volcanology*, *73*(2), 191-204.

Tibaldi, A. (2015), Structure of volcano plumbing systems: A review of multi-parametric effects, *Journal of Volcanology and Geothermal Research*, *298*, 85-135.

Tobita, M., M. Murakami, H. Nakagawa, H. Yarai, S. Fujiwara, and P. A. Rosen (2001), 3‐D surface deformation of the 2000 Usu eruption measured by matching of SAR images, *Geophysical Research Letters*, *28*(22), 4291-4294.

Vachon, R., and C. F. Hieronymus (2016), Effect of host-rock rheology on dyke shape, thickness, and magma overpressure, *Geophysical Journal International*, ggw448.

1037 Wright, T. J., C. Ebinger, J. Biggs, A. Ayele, G. Yirgu, D. Keir, and A. Stork (2006), Magma-
1038 maintained rift segmentation at continental rupture in the 2005 Afar dyking
1039 episode, *Nature*, *442*(7100), 291-294.

1040

1041

Figure 1.

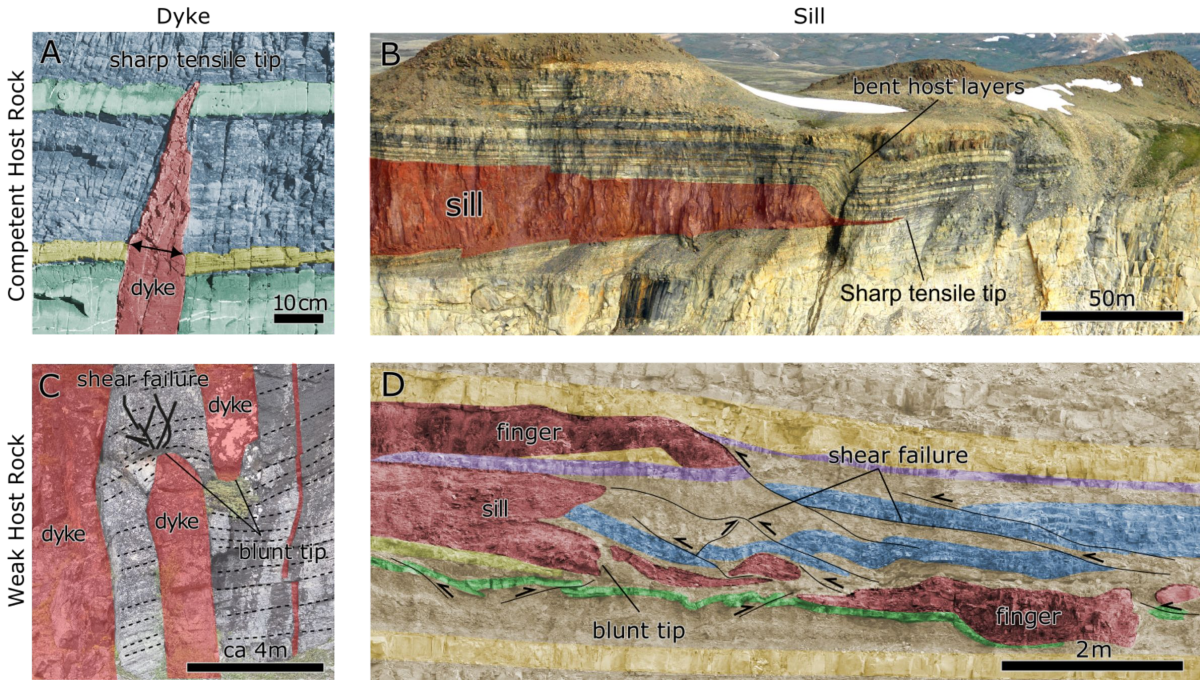
Dyke
Sill
Competent Host Rock
Weak Host Rock
A
sharp tensile tip
dyke
10 cm
B
bent host layers
sill
Sharp tensile tip
50m
C
shear failure
dyke
dyke
dyke
blunt tip
ca 4m
D
finger
shear failure
sill
blunt tip
finger
2m

Figure 2.

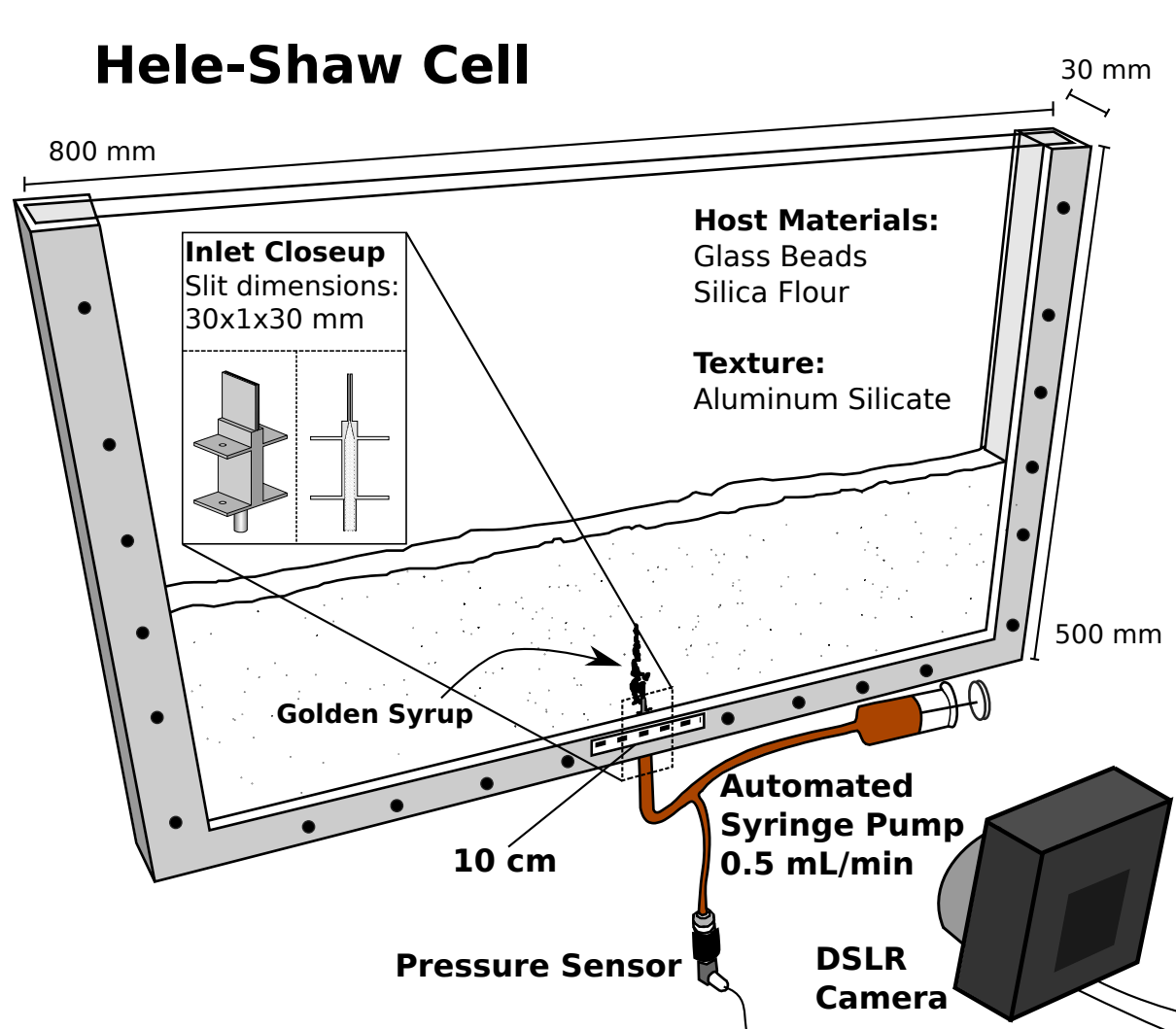
Hele-Shaw Cell
30 mm
800 mm
Inlet Closeup
Slit dimensions:
30x1x30 mm
Host Materials:
Glass Beads
Silica Flour
Texture:
Aluminum Silicate
500 mm
Golden Syrup
Automated
Syringe Pump
0.5 mL/min
10 cm
Pressure Sensor
DSLR
Camera

Figure 3.

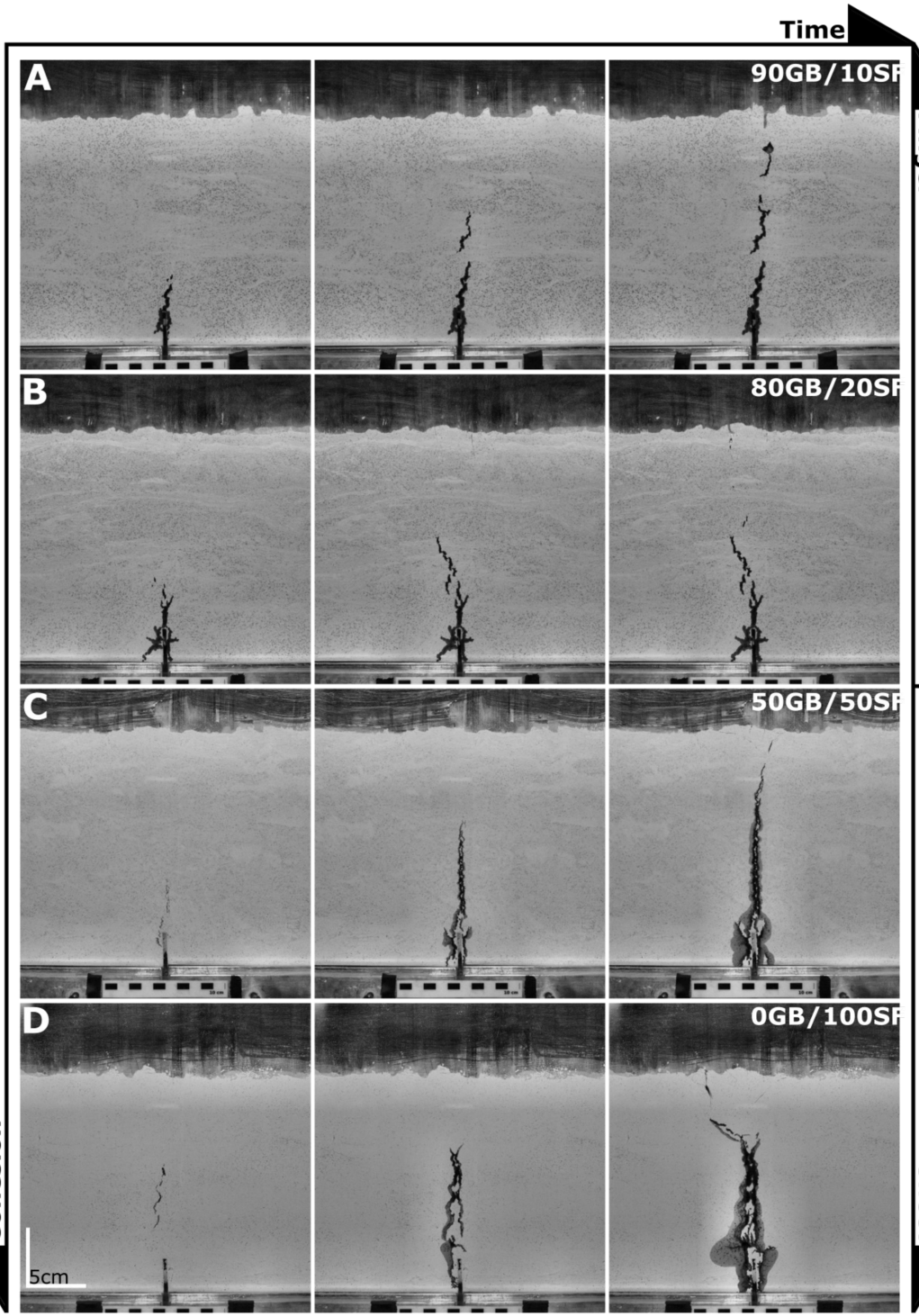
Time
Finger
Sheet
Cohesion
A
90GB/10SF
B
80GB/20SF
C
50GB/50SF
D
0GB/100SF
5cm

Figure 4.

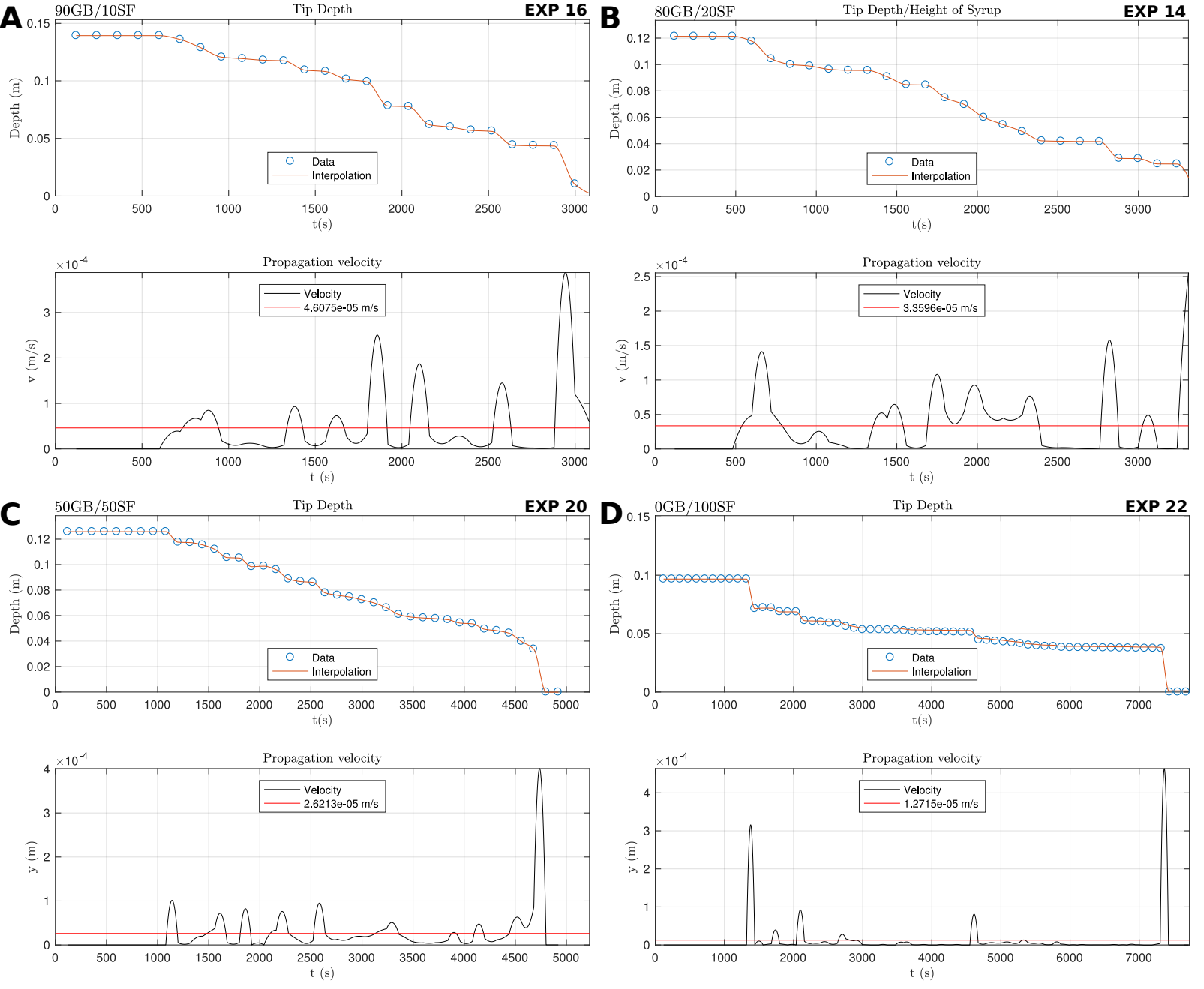
A
90GB/10SF
Tip Depth
EXP 16
Depth (m)
t(s)
Data
Interpolation
Propagation velocity
v (m/s)
t (s)
Velocity
4.6075e-05 m/s
B
80GB/20SF
Tip Depth/Height of Syrup
EXP 14
Depth (m)
t(s)
Data
Interpolation
Propagation velocity
v (m/s)
t (s)
Velocity
3.3596e-05 m/s
C
50GB/50SF
Tip Depth
EXP 20
Depth (m)
t(s)
Data
Interpolation
Propagation velocity
y (m)
t (s)
Velocity
2.6213e-05 m/s
D
0GB/100SF
Tip Depth
EXP 22
Depth (m)
t(s)
Data
Interpolation
Propagation velocity
y (m)
t (s)
Velocity
1.2715e-05 m/s

Figure 5.

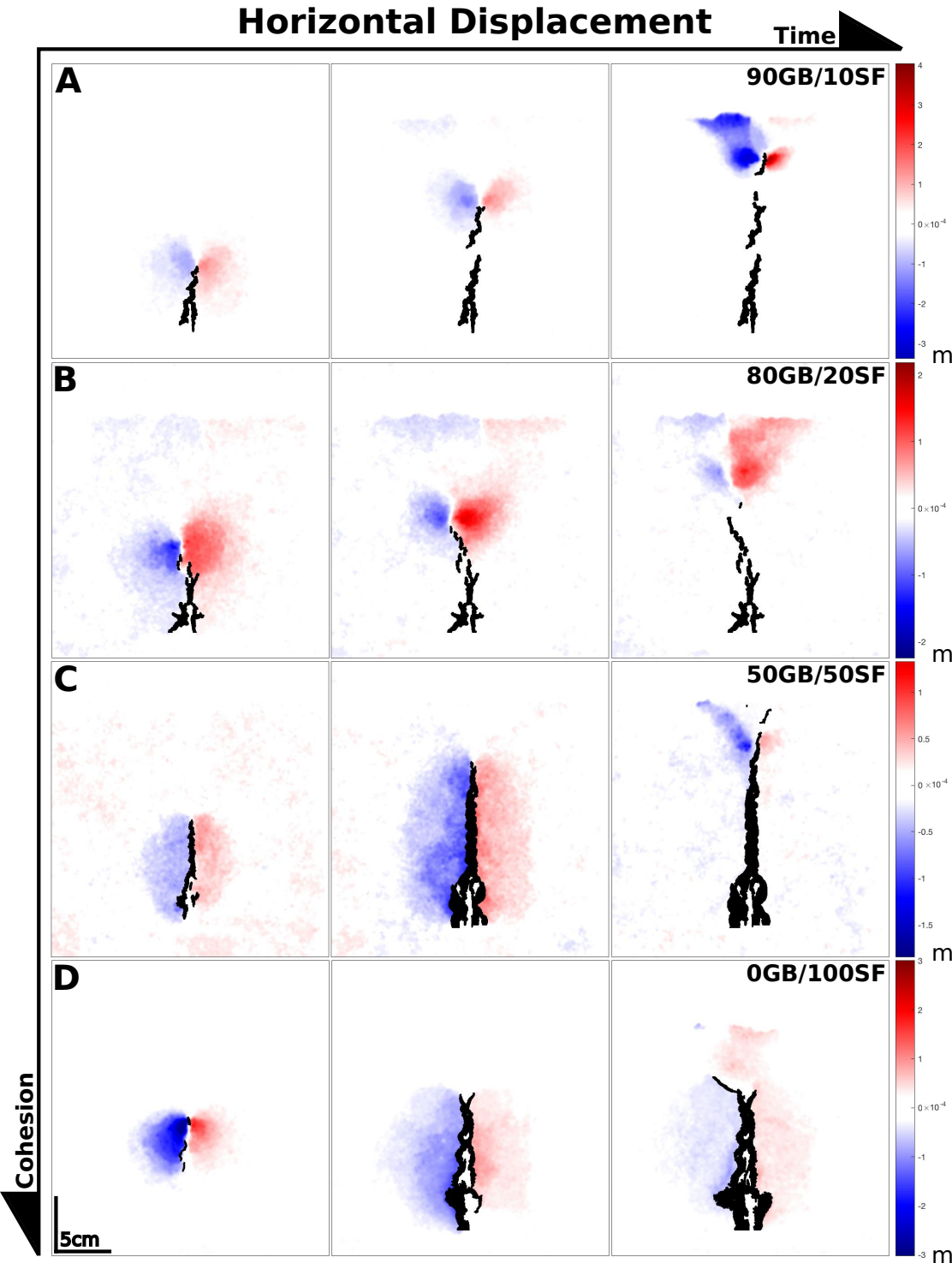
Horizontal Displacement
Time
Cohesion
A
90GB/10SF
B
80GB/20SF
C
50GB/50SF
D
0GB/100SF
5cm
m

Figure 6.

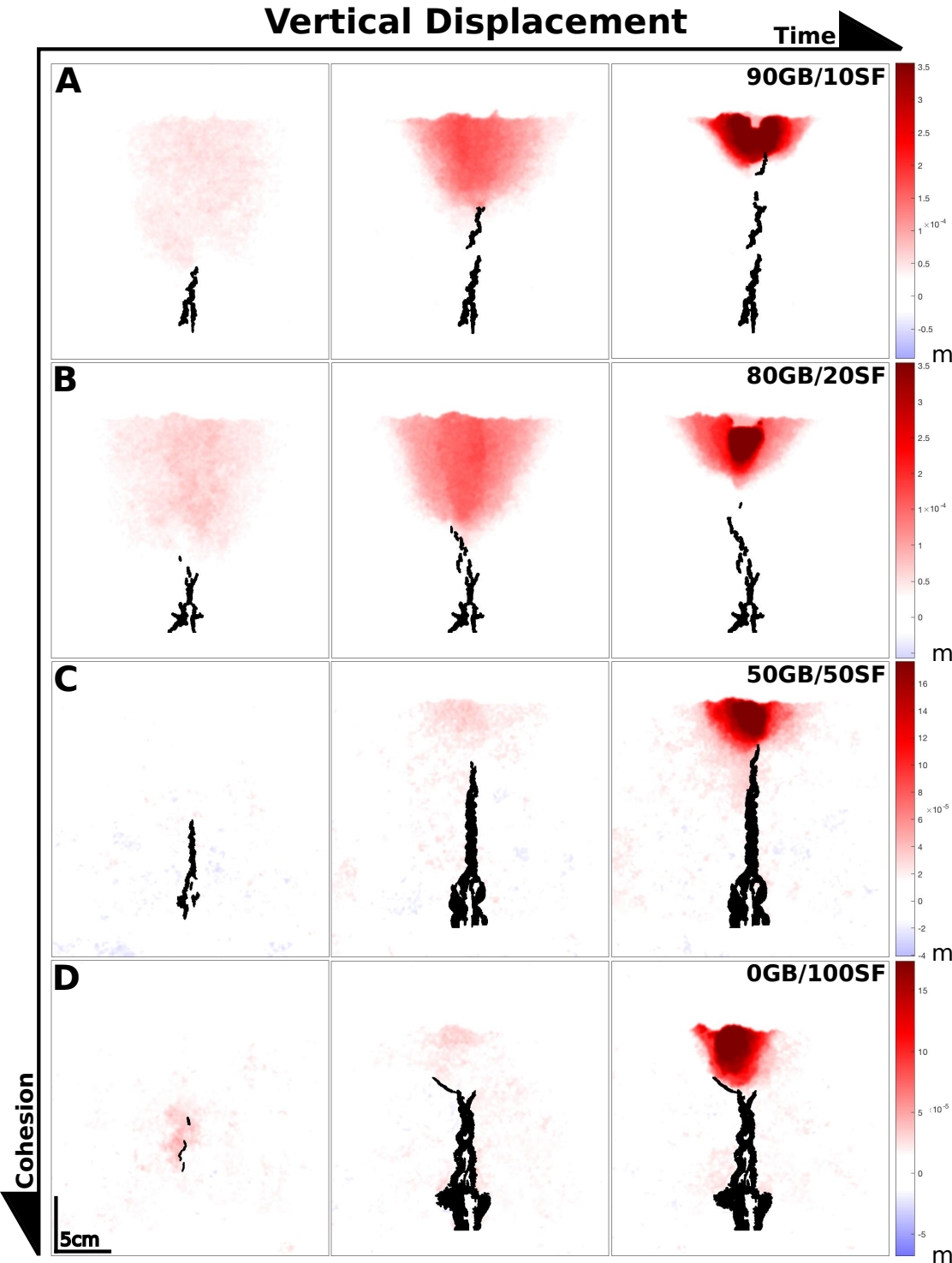
Vertical Displacement
Time
Cohesion
A
90GB/10SF
B
80GB/20SF
C
50GB/50SF
D
0GB/100SF
5cm
m

Figure 7.

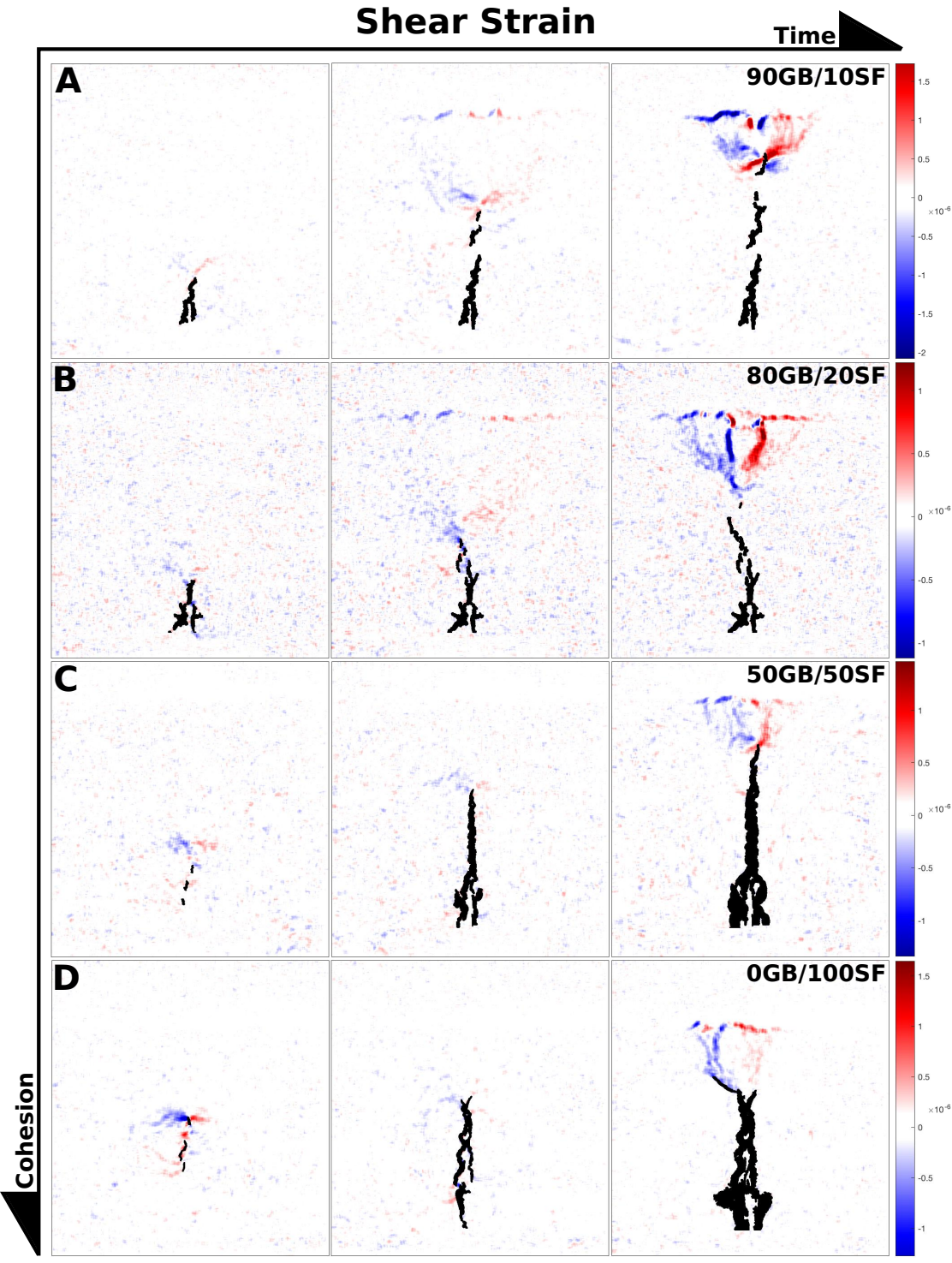
Shear Strain
Time
Cohesion
A
90GB/10SF
B
80GB/20SF
C
50GB/50SF
D
0GB/100SF
1.5
1
0.5
0
-0.5
-1
-1.5
-2
×10⁻⁶

Figure 8.

A

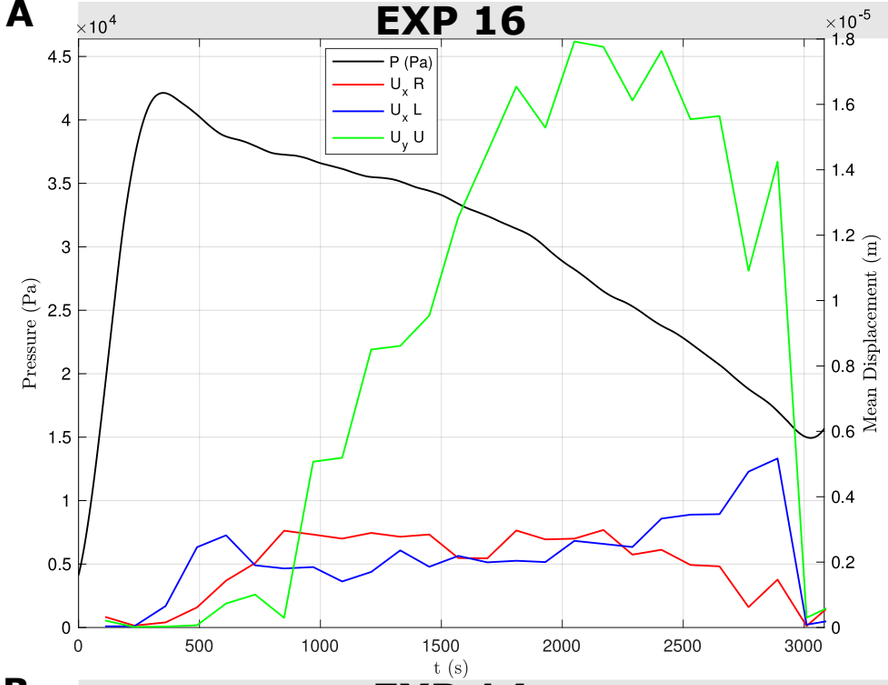
EXP 16
P (Pa)
U_x R
U_x L
U_y U
Pressure (Pa)
Mean Displacement (m)
t (s)

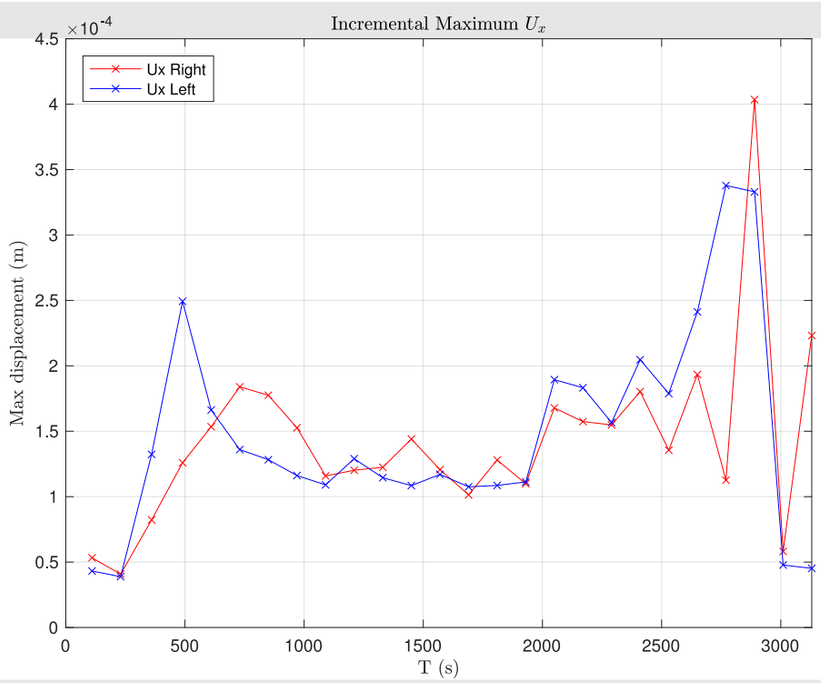
Incremental Maximum U_x
Ux Right
Ux Left
Max displacement (m)
T (s)

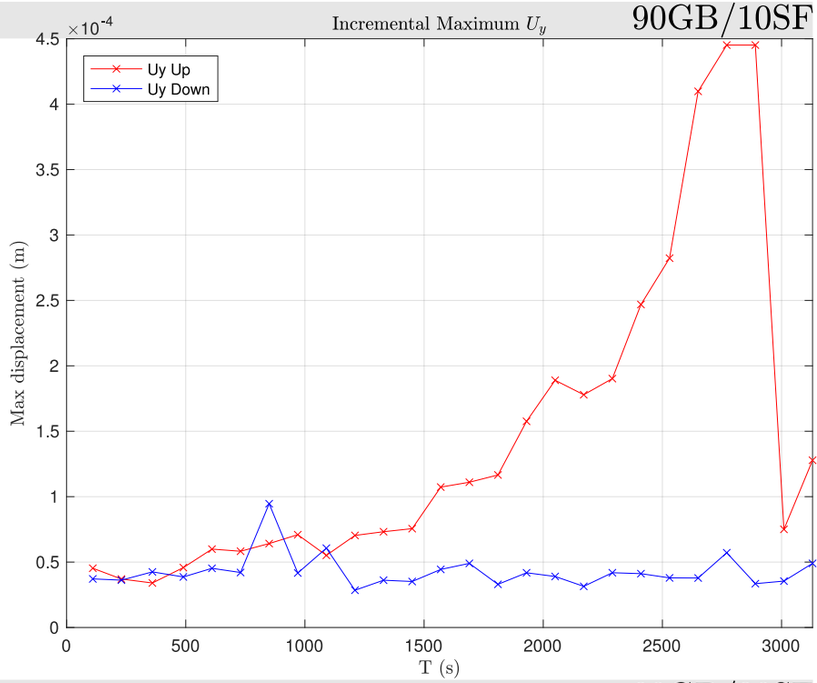
Incremental Maximum U_y
90GB/10SF
Uy Up
Uy Down
Max displacement (m)
T (s)

B

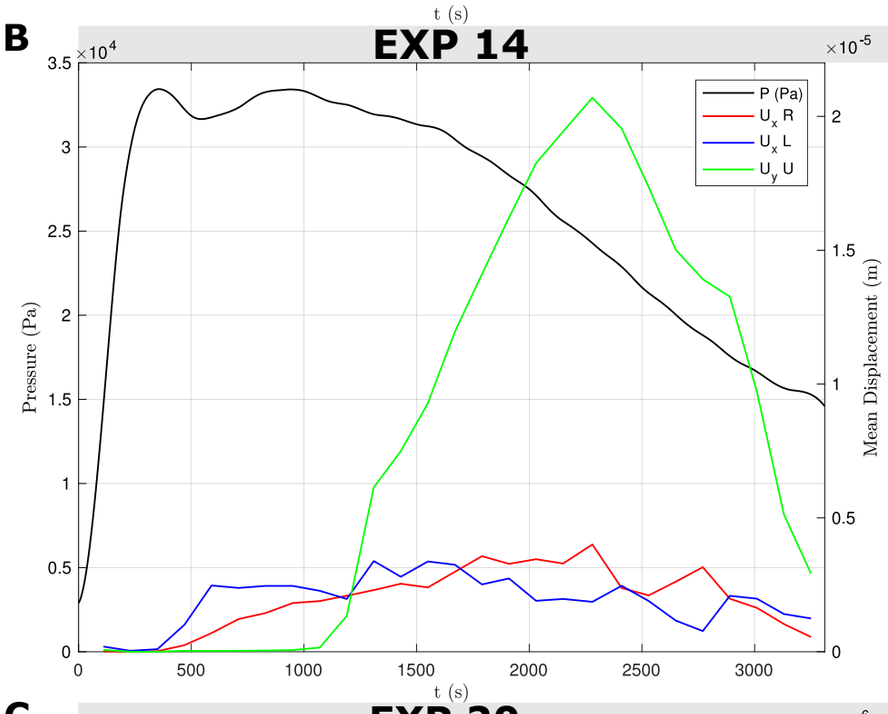
EXP 14
P (Pa)
U_x R
U_x L
U_y U
Pressure (Pa)
Mean Displacement (m)
t (s)

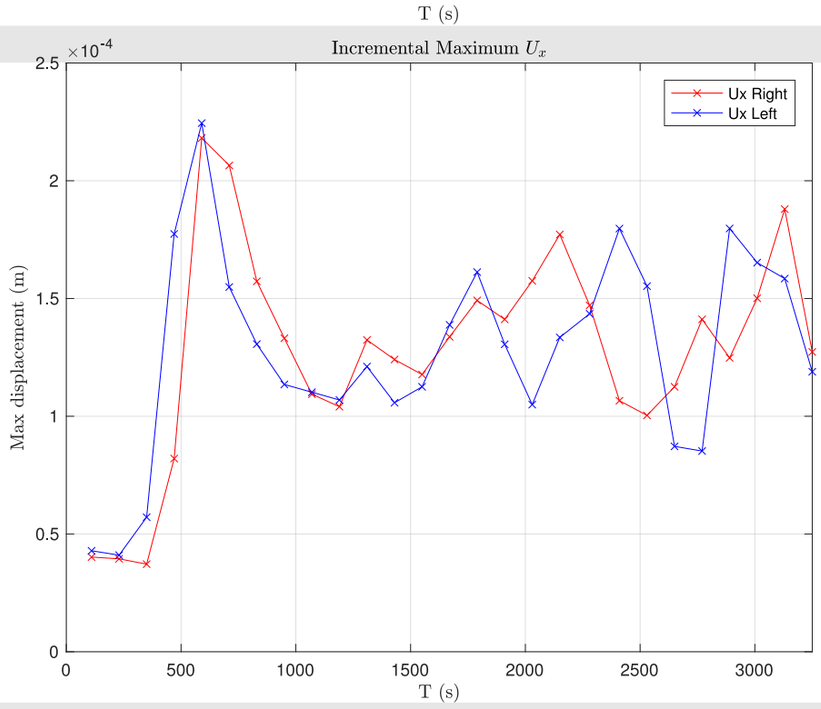
Incremental Maximum U_x
Ux Right
Ux Left
Max displacement (m)
T (s)

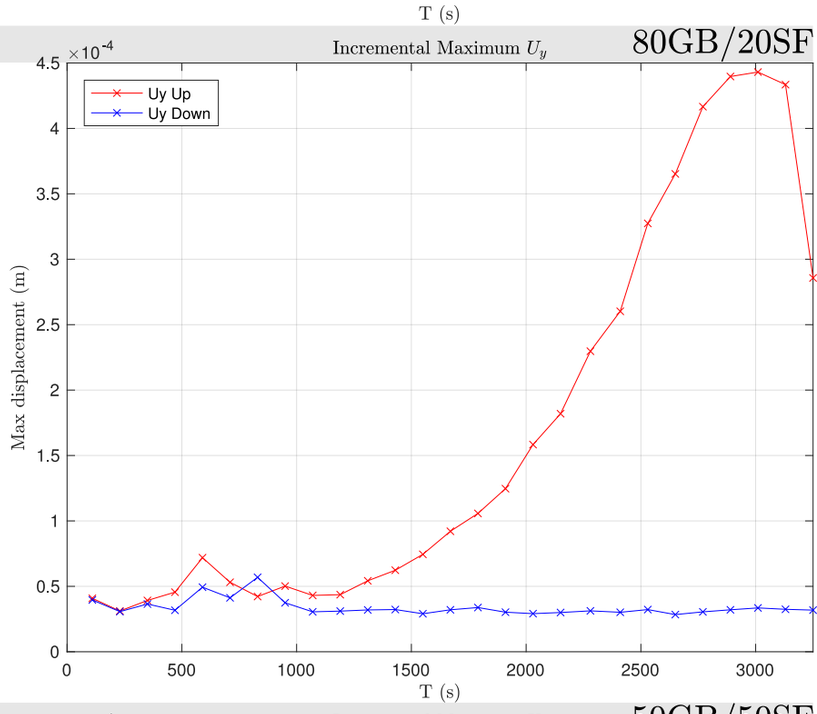
Incremental Maximum U_y
80GB/20SF
Uy Up
Uy Down
Max displacement (m)
T (s)

C

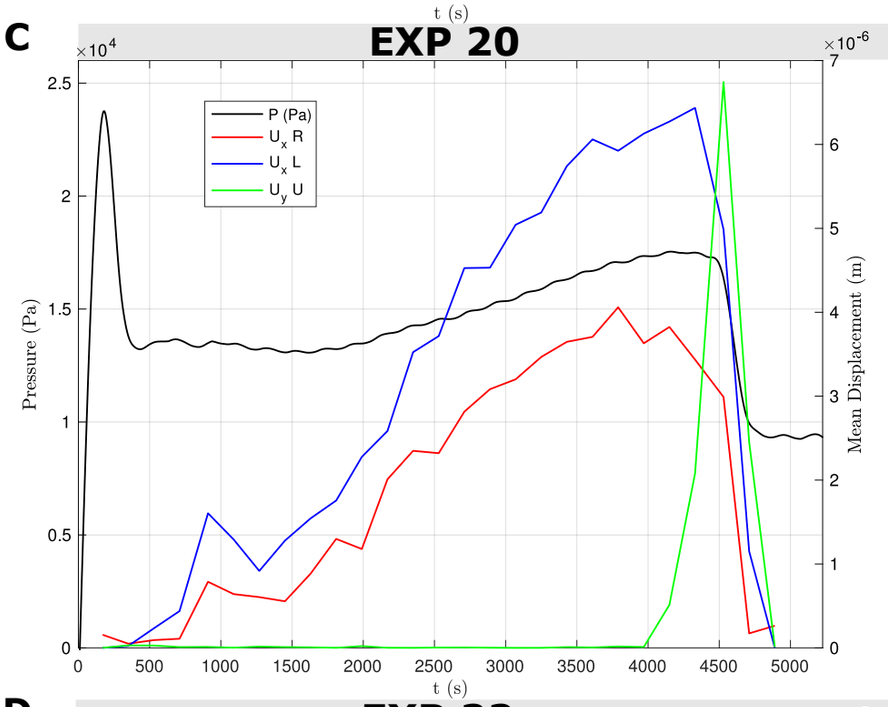
EXP 20
P (Pa)
U_x R
U_x L
U_y U
Pressure (Pa)
Mean Displacement (m)
t (s)

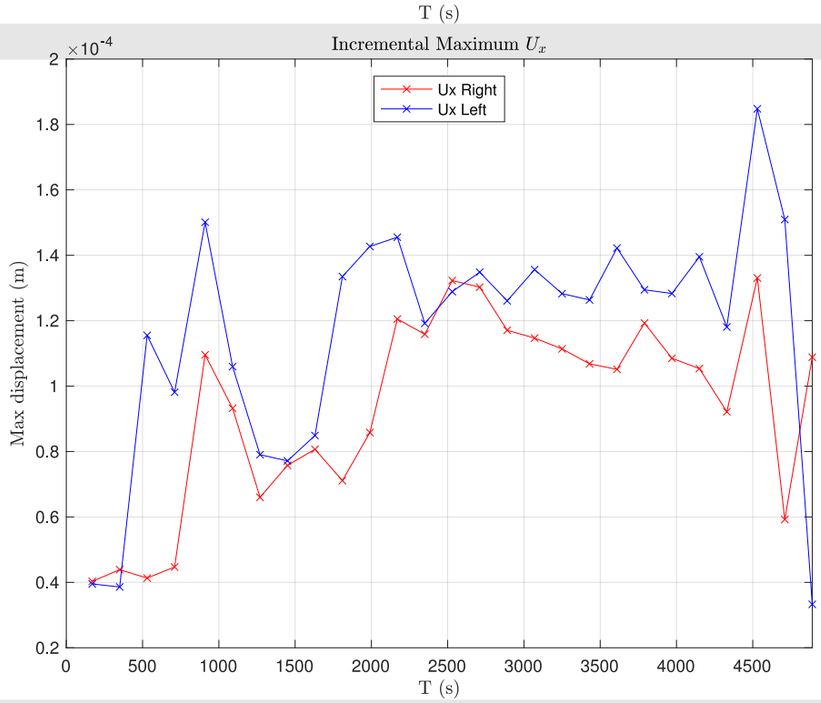
Incremental Maximum U_x
Ux Right
Ux Left
Max displacement (m)
T (s)

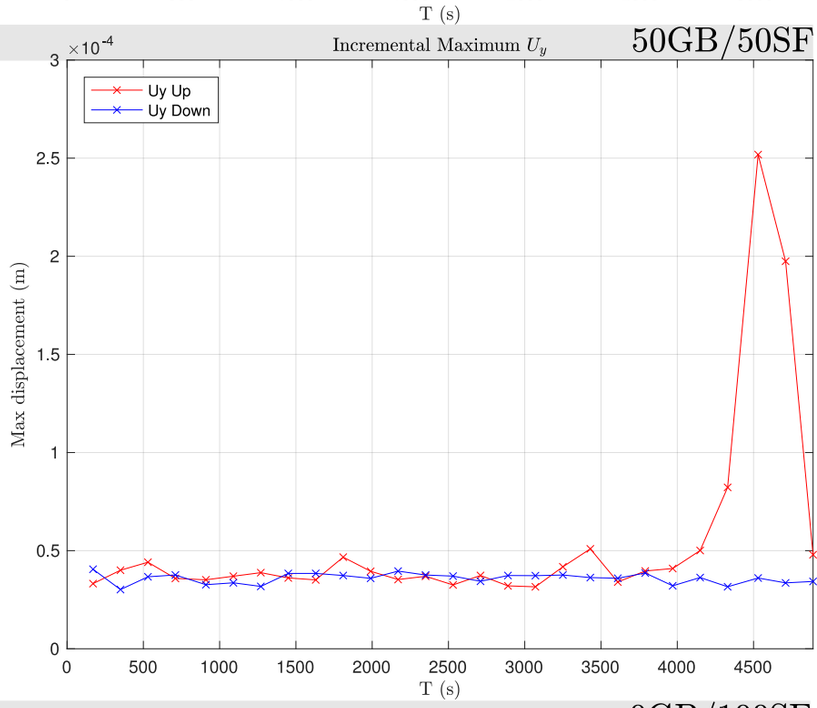
Incremental Maximum U_y
50GB/50SF
Uy Up
Uy Down
Max displacement (m)
T (s)

D

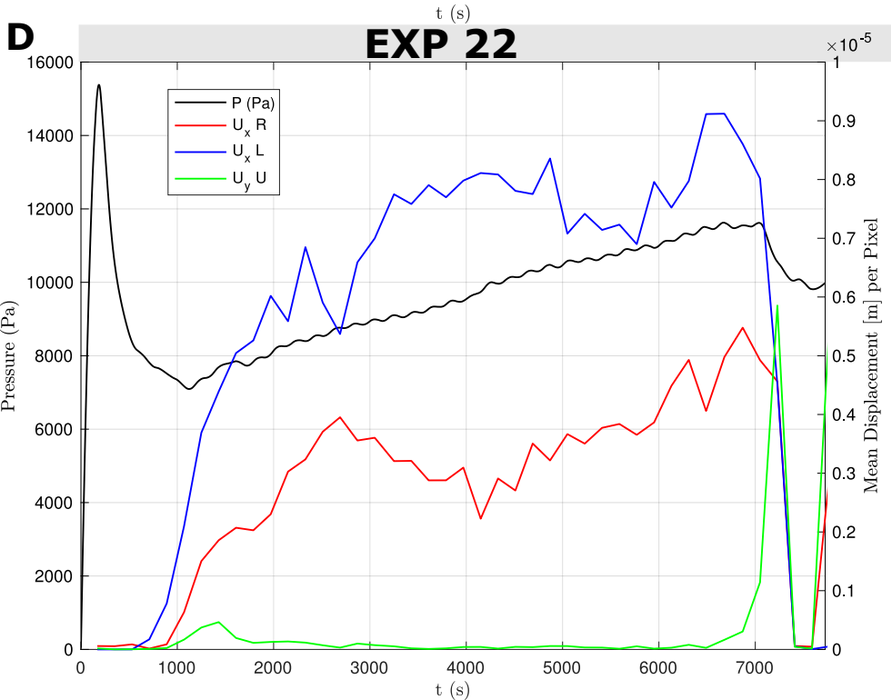
EXP 22
P (Pa)
U_x R
U_x L
U_y U
Pressure (Pa)
Mean Displacement [m] per Pixel
t (s)

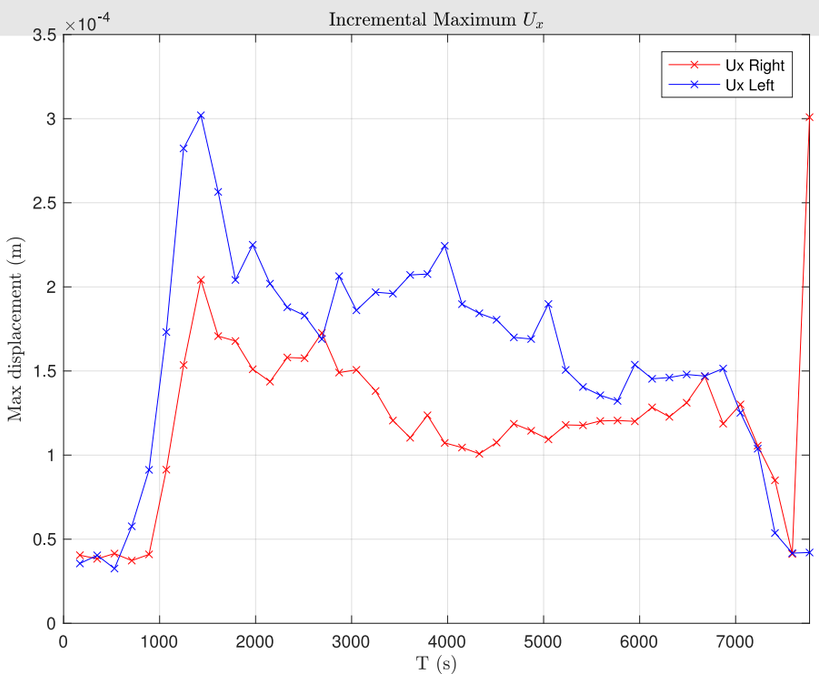
Incremental Maximum U_x
Ux Right
Ux Left
Max displacement (m)
T (s)

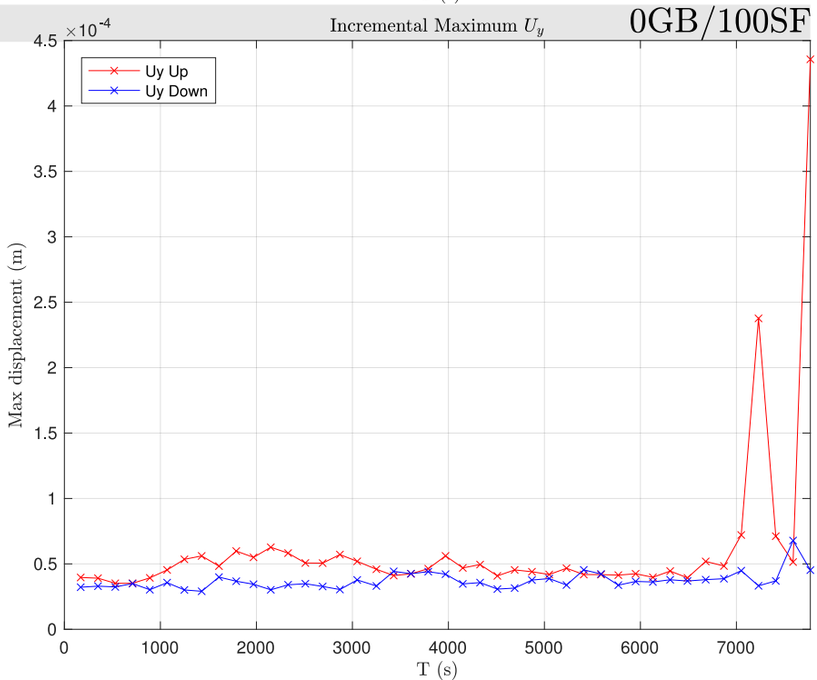
Incremental Maximum U_y
0GB/100SF
Uy Up
Uy Down
Max displacement (m)
T (s)

Figure 9.

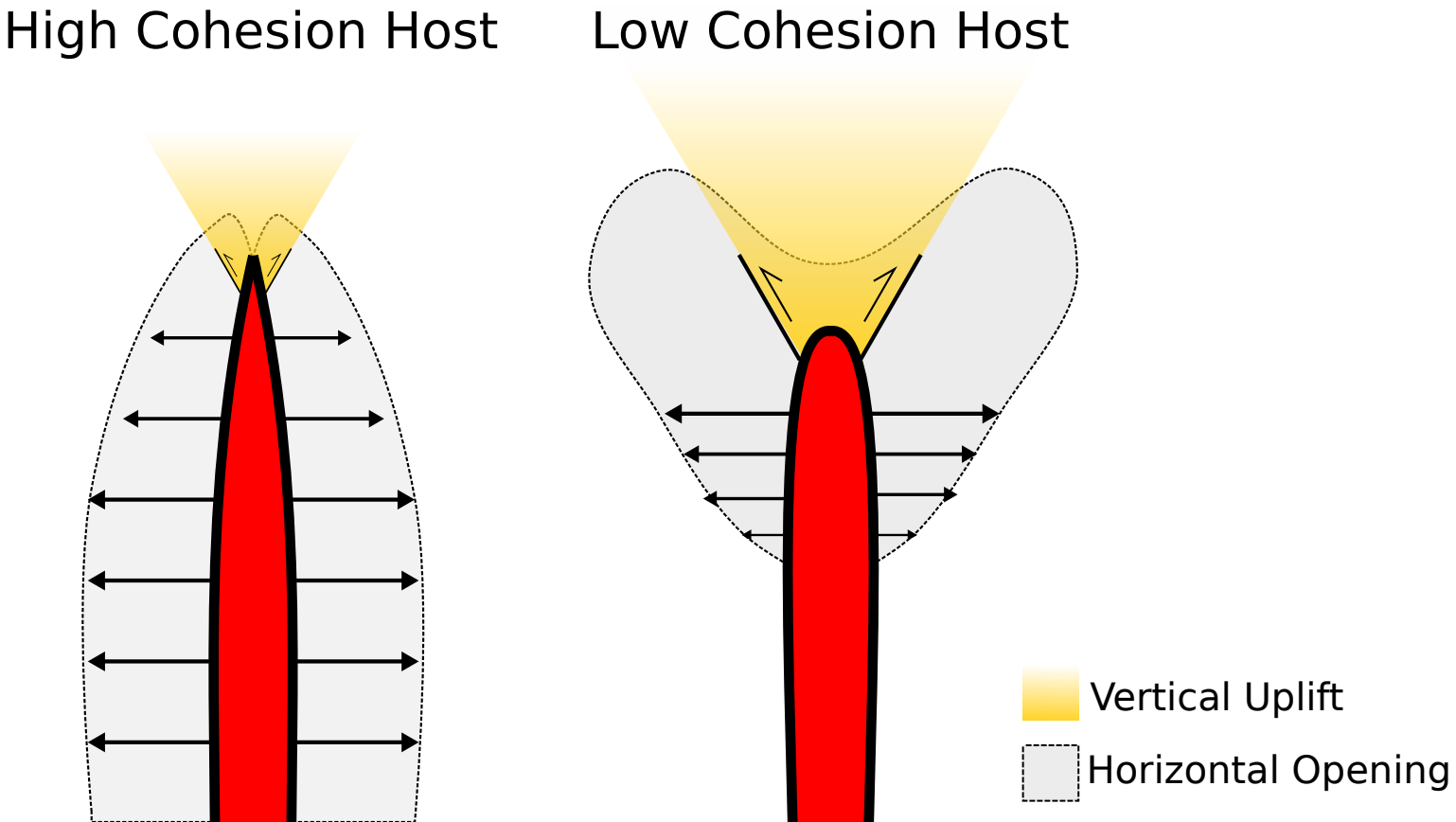
High Cohesion Host
Low Cohesion Host
Vertical Uplift
Horizontal Opening